



Li, W., Yu, Z., Wang, Y. and Li, Y. (2022) Heat transfer of supercritical carbon dioxide in a tube-in-tube heat exchanger-a CFD study. *Journal of Supercritical Fluids*, 181, 105493.

There may be differences between this version and the published version. You are advised to consult the publisher's version if you wish to cite from it.

<https://eprints.gla.ac.uk/259124/>

Deposited on: 22 November 2021

Enlighten – Research publications by members of the University of Glasgow
<https://eprints.gla.ac.uk>

Heat Transfer of Supercritical Carbon Dioxide in a Tube-in-Tube Heat Exchanger-A CFD Study

Wenguang Li¹, Zhibin Yu^{1*}, Yi Wang², and Yongliang Li²

¹ School of Engineering, University of Glasgow, G12 8QQ, Glasgow, UK

² School of Chemical Engineering, University of Birmingham, B15 2TT, Birmingham, UK

*The correspondence E-mail: Zhibin.Yu@glasgow.ac.uk (Zhibin Yu)

The other E-mail: Wenguang.Li@glasgow.ac.uk (Wenguang Li),

Tel: +44-0141330530

Date: 22 November 2021

Abstract

For better design and optimization of the heat exchanger (HX), forced convective heat transfer and flow characteristics of supercritical carbon dioxide (SCO₂) in a water-cooled experimental counter-flow tube-in-tube HX were studied numerically with three-dimensional Reynolds-averaged Navier-Stokes equations and shear stress transport (SST) turbulence model by using computational fluid dynamics method in ANSYS CFX. With a sole tube model of the HX, effects of SCO₂ inlet pressure, mass flux, tube diameter and wall heat flux on SCO₂ mean heat transfer coefficient (MHTC) were investigated. Influences of turbulence models and discretisation schemes of the advection terms in the SST model, wall temperature of conservative and hybrid values in CFX-Post on MHTC were clarified, and buoyancy effect in the horizontal HX was explored. The SST model can achieve better agreement with the experimental MHTCs of SCO₂ than the other models. The buoyancy effect can improve MHTC by the secondary flows in the tube.

Keywords: supercritical carbon dioxide; tube-in-tube heat exchanger; heat transfer coefficient; forced convective heat transfer; buoyancy effect; computational fluid dynamics

Nomenclature

a	constant in the μ_t expression of the shear stress transport model, $a=0.31$
B	constant in log-law velocity profile, $B=5.2$ for hydraulically smooth walls
C_p	specific heat capacity of fluid, J/kg
d	inner diameter, mm
f	variable related to energy redistribution
F_1	blending function between the Wilcox $k-\omega$ model and the standard $k-\varepsilon$ model
F_2	auxiliary variable in the μ_t expression of the shear stress transport model
g_i	components of the acceleration of gravity, $i=1, 2, 3$, m/s ²
G	mass flux, kg/m ² s
Gr_b	Grashof number
h	specific enthalpy of fluid, m ² /s ²
k	turbulence kinetic energy, m ² /s ²
n	power relating to tube orientation
p	fluid static pressure, MPa
$P_{kb}, P_{\omega b}$	buoyancy production term in the k -equation and ω -equation, respectively, J/m ³
Pr	fluid Prandtl number
Pr_t	turbulent Prandtl number, $Pr_t=0.9$
q_w	water heat flux across the tube wall, kW/m ²
Re	Reynolds number at inlet of the tube
Re_b	Reynolds number based on bulk velocity in the tube
Ri	Richardson number
S_E	source term of energy equation, J/m ³
S_i	specific body force, $i=1, 2, 3$, m/s ²
t	time, s
T	local temperature of fluid, °C, K
T_0	reference temperature of fluid, °C, K
T_1	fluid temperature at inlet of the tube, °C, K
T_b	mean bulk temperature of fluid, °C, K
T_c	temperature at pseudo critical point of fluid, °C, K
T_n	fluid temperature in the first mesh layer, °C, K
T^+	dimensionless temperature in the boundary layer
T'	fluctuation of fluid temperature, K
u_b	bulk velocity of fluid in the tube, m/s
u_i, u_j	Reynolds time-averaged velocity components of fluid in a Cartesian coordinate system, $i, j=1,2, 3$, m/s

u_n	fluid velocity near wall, m/s
u'_i	turbulent fluctuation velocity of fluid, m/s
u_τ	friction velocity of fluid at wall, $u_\tau = \sqrt{\tau_w/\rho}$, m/s
$u_\tau^{log}, u_\tau^{vis}$	friction velocities at wall by using the solutions in the log-law and sublayer layers
U	mean heat transfer coefficient, W/m ² K
v^2	velocity scale for turbulence transport, m ² /s ²
x_i, x_j	coordinates of a Cartesian coordinate system, $i, j=1, 2, 3$, m
y_n	distance to the nearest wall from the first mesh layer, m
y^+	dimensionless wall distance, $y^+ = \sqrt{\tau_w/\rho} y_n/\nu$

Greek

$\alpha_1, \beta_1, \sigma_{\omega 1}$	model constants in the ω -equation of the Wilcox k - ω model, $\alpha_1=5/9, \beta_1=0.075, \sigma_{\omega 1}=2$
$\alpha_2, \beta_2, \sigma_{\omega 2}$	model constants in the ω -equation of the ω -transformed standard k - ε model, $\alpha_2=0.44, \beta_2=0.0828, \sigma_{\omega 2}=1/0.856$
$\alpha_3, \beta_3, e, \sigma_{\omega 3}$	blended model constants in the ω -equation of the blended Wilcox k - ω and standard k - ε models, $\alpha_3=F_1\alpha_1+(1-F_1)\alpha_2, \beta_3=F_1\beta_1+(1-F_1)\beta_2, \sigma_{\omega 3}=F_1\sigma_{\omega 1}+(1-F_1)\sigma_{\omega 2}$
β	auxiliar variable in dimensionless fluid temperature expression in the boundary layer
β_k	model constant in the k -equation of the Wilcox k - ω model and the ω -transformed standard k - ε model, $\beta_k=0.09$
β_v	volumetric thermal expansion coefficient of fluid, 1/K
γ	magnitude of the strain rate of fluid velocity, 1/s
γ_{ij}	strain rate tensor of fluid velocity, 1/s
Γ	auxiliary variable dimensionless fluid temperature in boundary layer
ε	dissipation rate of turbulence kinetic energy, m ² /s ³
ζ_t	turbulent thermal diffusivity, m ² /s
κ	von Kármán constant, $\kappa=0.41$
λ	thermal conductivity of fluid, W/m K
μ	molecular dynamic viscosity of fluid, Pa.s
μ_t	turbulent eddy viscosity, Pa.s
ν	molecular kinematic viscosity of fluid, m ² /s
ξ_1, ξ_2	auxiliary variables in the F_1 expressions
ξ_3	auxiliary variable in the μ_t expression of the shear stress transport model
ρ	density of fluid, kg/m ³
ρ_0	reference density of fluid, kg/m ³

σ_{k1}	model constant in the k -equation of the Wilcox k - ω model, $\sigma_{k1}=2$
σ_{k2}	model constant in the k -equation of the standard k - ε model, $\sigma_{k2}=1$
σ_{k3}	blended model constant in the k -equation of the blended Wilcox k - ω and standard k - ε models, $\sigma_{k3}=F_1\sigma_{k1}+\beta_1(1-F_1)\sigma_{k2}$
τ_w	wall shear stress, Pa
ω	rate of dissipation per unit turbulent kinetic energy, 1/s
ω_1	total ω near wall, 1/s
$\omega_{log}, \omega_{vis}$	ω values calculated by the solutions in the logarithmic and linear near-wall regions, 1/s

Subscript

i, j index of the Cartesian coordinate system

Abbreviation

1D	one-dimensional
2D	two-dimensional
3D	three-dimensional
BLS	baseline
CFD	computational fluid dynamics
CO2	carbon dioxide
DNS	direct numerical simulation
HX	heat exchanger
LES	large eddy simulation
MHTC	mean heat transfer coefficient
RANS	Reynolds-averaged Navier-Stokes equations
RGP	real gas property
RNG	renormalisation group
SCO2	supercritical carbon dioxide
SST	shear stress transport
std	standard deviation

1 Introduction

Cooling is one of the key energy consumers. Cooling consumes up to 14% of the UK's electricity, and the cooling demand will grow by about three folds the current generating capacity by 2030 in the UK [1]. The recycling of waste cold and the storing of cold energy produced by excess renewable energy power generated at night can be a practical solution to provide low-carbon, zero-emission cooling and power. In this context, a combined cooling and cold storage system using carbon dioxide (CO₂) hydrate slurry as both working fluid and storage medium was proposed by us in a granted project. A water-cooled supercritical carbon dioxide (SCO₂) heat exchanger (HX) will be used in the system, thus SCO₂ heat transfer needs to be enhanced to improve its effectiveness and compactness [2]. The prediction of the thermo-hydraulic performance of heat transfer enhancement under SCO₂ flow conditions based on computational fluid dynamics (CFD) will play a key role in SCO₂ HX design and optimization. As the first step, the convective heat transfer in a water-cooled experimental SCO₂ tube-in-tube HX was investigated by using CFD approach to establish a numerical method and validate heat transfer and fluid flow models under the condition where the thermophysical and transport properties vary significantly with temperature and pressure.

Numerical analysis of turbulent flows of SCO₂ with forced convective heat transfer in a tube started in the 1960s. The methods used in the numerical analysis can be classified into five groups: (1) one-dimensional (1D) analytical Reynolds-averaged Navier-Stokes equations (RANS) method, (2) two-dimensional (2D) RANS method, (3) three-dimensional (3D) RANS method; (4) large eddy simulation (LES) method; (5) direct numerical simulation (DNS) method. In the 1D RANS method, SCO₂ is considered as a viscous compressible fluid and its steady flow in a tube is axisymmetric, turbulent, and fully developed. As a result, the flow is simplified to a 1D flow in the tube radial direction only, i.e., the continuity, momentum, energy equations are as functions of radius only. In the 2D RANS method, the steady flow of viscous compressible SCO₂ is turbulent and axisymmetric, but not fully developed in a tube, thus the variation of fluid velocity and temperature along the tube can be characterized. The finite difference or finite volume approach was employed to solve 2D steady time-averaged compressible Navier-Stokes equations and energy equation as well as turbulence closure model by using in-house computer programs. In the 3D RANS method, the flow of viscous compressible SCO₂ is 3D and turbulent with buoyancy effect in a tube. The finite volume method and general CFD software, namely Fluent or CFX, were used. In the LES method, the unsteady, compressible Navier-Stokes equations and energy equation of SCO₂ in microchannels were solved with LES turbulence models accounting for turbulence contributions to momentum and thermal energy transport, respectively. For the DNS method, the unsteady, compressible Navier-Stokes equations or its low-Mach-number form and the energy equation of SCO₂ in a tube were solved directly by using an in-house computer

program or the open-source finite volume code OpenFOAM without any turbulence closure models.

Compared with 1D RANS, 2D RANS, LES and DNS methods, the use of 3D RANS method is a trade-off between accuracy and time-consumption in HX design, hydraulic and thermal performance estimation. Additionally, it is well-known that the 3D RANS method can capture the heat transfer deterioration effect. Therefore, this method is adopted here.

In the 3D RANS method, the standard $k-\varepsilon$ model with low Reynolds number corrections [3] [4] [5], SST model [6] [7] [8] [9] [10], and 4-equation eddy viscosity model of $k-\varepsilon-v^2-f$ [11] as well as turbulent stress tensor (elliptic blending second-moment closure)- ε model [12] have been examined in SCO₂ heat transfer simulations. The standard $k-\varepsilon$ model with the Lam–Bremhorst correction [3] or Abe-Kondoh-Nagano correction [4] [5] leads to the best agreement with the experimental mean heat transfer coefficient (MHTC). The SST model performs better than the realizable $k-\varepsilon$ model with enhanced wall treatment in accuracy and computational efficiency [6]. The SST model is better than the $k-\omega$ model in bulk flow and the $k-\varepsilon$ model in computational accuracy near wall region [7]. There is no comparison between the SST model and the other models [8] [9] [10]. The 4-equation eddy viscosity model of $k-\varepsilon-v^2-f$ model was compared with DNS and the fair agreement in Nusselt number was achieved between the two models [11]. The Reynolds stress spanwise profile and SCO₂ MHTC curve predicted by the turbulent stress tensor- ε model agree better with the measurement than the Reynolds stress models proposed by Shin et al, and Dol et al [12]. A comparison was made among the standard $k-\varepsilon$ model, RNG $k-\varepsilon$ model, $k-\varepsilon$ model with low Reynolds number correction, $k-\omega$ model and SST model in terms of SCO₂ MHTC at tube wall, and it was demonstrated that the standard $k-\varepsilon$ model with enhanced wall treatment results in the best agreement with the experimental MHTC [13]. In [14], the standard $k-\varepsilon$ and RNG $k-\varepsilon$ models were compared in terms of both SCO₂ MHTC and wall temperature, suggesting the RNG $k-\varepsilon$ model is better than the standard $k-\varepsilon$ model. Obviously, whether the standard $k-\varepsilon$ and RNG $k-\varepsilon$ models are better than the SST model for simulating SCO₂ convective heat transfer in the tube-in-tube HX needs to be confirmed further.

In the present article, the convective heat transfer of SCO₂ in a water-cooled tube-in-tube HX is investigated based on CFD simulations in ANSYS CFX 2019R2 by using 3D RANS method with the shear stress transport (SST) turbulence model. A complete geometrical model and a sole tube geometrical model for the HX were generated, the forced convective heat transfer of SCO₂ in the models are simulated, and the sole tube geometrical model was chosen over the complete geometrical model based on simulation practice. Effects of SCO₂ mass flux (200, 400, 600kg/m²s), tube diameter (4, 6mm), inlet pressure (8, 9MPa), wall heat flux (6, 12, 24, 33kW/m²), numerical scheme for advection terms in the SST model equations, conservative and hybrid values of tube wall temperature on the MHTC profiles of SCO₂ were

clarified and compared with the MHTC of SCO₂ obtained in heat transfer experiments on the HX [15]. The effects of the other turbulence models such as the eddy transport, standard k - ϵ , renormalization group (RNG) k - ϵ , Wilcox k - ω , baseline (BLS) k - ω and ω -stress turbulence models in [16] were also investigated. The buoyancy effect was discussed.

Such a detailed CFD study on convective heat transfer of SCO₂ in tube-in-tube HXs has not been seen in the literature so far. The article can provide guidelines for the selection of appropriate geometrical models, flow models and numerical schemes as well as the assessment of buoyancy effect for CFD simulations, but also deliver an understanding of the complex SCO₂ heat transfer phenomenon in the HX. Particularly, the unique thermophysical and transport property variations and the buoyancy effect in SCO₂ heat transfer were considered.

2 Methodology

2.1 The geometrical models

There are several experiments on heat transfer in water-cooled tube-in-tube SCO₂ HXs. Unfortunately, most of them cannot be employed to validate SCO₂ flow models and numerical methods due to the lack of detailed geometrical parameters and experimental conditions. Thus, the counter-flow tube-in-tube SCO₂ HX in [15] has to be chosen in the article. The schematic of the experimental set-up and the axial-cross-sectional view of the tube-in-tube SCO₂ HX, geometrical dimensions of the HX, a brief on experimental procedure and the experimental conditions are outlined in Appendix A.

According to the geometrical dimensions of the counter-flow tube-in-tube HX shown in Appendix A, two geometrical models, i.e., complete model, and sole tube model, as shown in Figure 1, were built and examined. Since the HX structure is geometrically symmetric, only half of the HX was employed in the two models. The complete model consists of a 1mm thick inner tube with $15d$ long upstream and downstream extensions, and an annulus with 50mm long, 6mm diameter upstream and downstream branches. The outer surfaces of the annulus and the two extensions are insulated and adiabatic. In this model, both the water temperature at the annulus inlet and the water flow rate were not provided in [15], and thus must be guessed to meet a known constant experimental wall heat flux across the inner tube wall from the hot SCO₂ to the cold water in [15] in a SCO₂ heat transfer simulation.

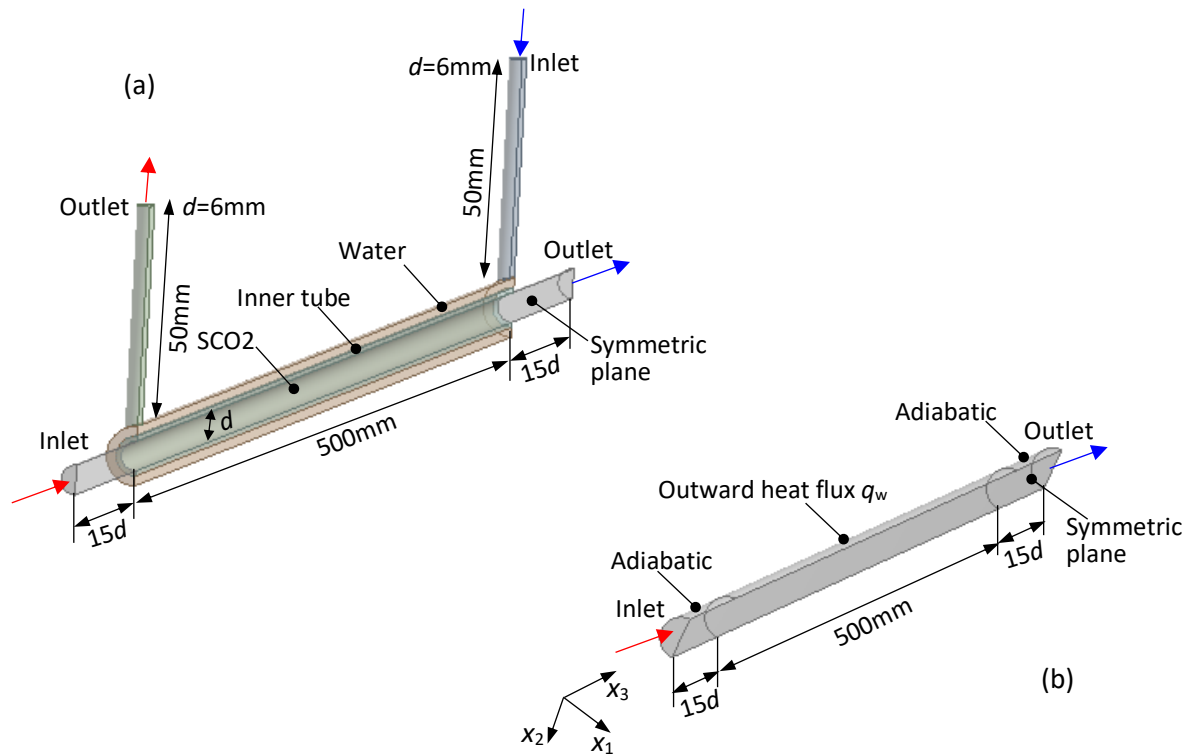


Figure 1 Two geometrical models of the water-cooled SCO₂ counter-flow tube-in-tube HX in [15], (a) complete model, (b) sole tube model, the inner tube and two branches share the same inner diameter

Initial CFD simulations proved that the complete geometrical model was considerably time-consuming and succeeded in one case only. It was very difficult to guess a series of correct water flow rates and inlet temperatures for a known wall heat flux in the simulations, and the water inlet temperature could influence the inner wall temperature subsequently the SCO₂ MHTC sustainably. Thus, the sole tube model has to be tried then. In the sole tube model, the annulus is removed, and the water-cooling effect on the hot SCO₂ is reproduced with a known constant experimental outward heat flux q_w . This model requires SCO₂ inlet temperature and pressure only, and the experimental outward heat flux q_w is imposed as a boundary condition, hence, the computational time of this model is significantly reduced. In the following sections, all the results are obtained by using the sole tube model, but the difference in the heat transfer between the two geometrical models will be analysed in the discussion section late on.

2.2 The fluid flow and heat transfer models

The CFD software ANSYS 2019R2 CFX is employed to conduct SCO₂ heat transfer simulations. The SCO₂ in CFD simulations is treated as subsonic compressible gas and its thermophysical and transport properties vary with both temperature and pressure. Ten SCO₂ thermophysical and transport property constants were calculated by using the REFPROP Version 9.0 program issued by the National Institute of Standards and Technology. Then, the values of these property constants were read into a custom MATLAB program to generate the

real gas property (RGP) table file based on the TASCflow (early version of CFX) RGP format provided in [17]. The file was read in Materials Tab in CFX-Pre by specifying a new material-SCO₂ and the location and name of the RGP file on the hard drive. Based on the RGP table, the SCO₂ thermophysical and transport property constants will be interpolated with local temperature and pressure in the fluid domain during a CFD simulation.

The SCO₂ flow and heat transfer models, which are adopted in the paper, include the 3D RANS equations, energy equation and SST turbulence model. The details of these equations and models are present in Appendix B.

2.3 The boundary conditions and initialization

In CFD heat transfer simulations, a couple of boundary conditions and one initialization condition are needed. In CFX, mass flow rate, pressure and temperature cannot be imposed simultaneously at the inlet; as such the pressure and temperature are given at the inlet, and the mass flow rate has to be assigned at the outlet.

In the complete model, the pressure and temperature of SCO₂ are imposed, the flow direction option is zero gradient, and the turbulence intensity is 5%, at the inlet of the inner tube. At the outlet of the tube, the flow of SCO₂ is subsonic and its mass flow rate is specified based on the prescribed SCO₂ mass flux and the cross-section area of the inner tube with the CFX expression language. The walls of the inner tube, two branches and annulus are subject to velocity no-slip condition and symmetrical boundary condition is imposed on the symmetrical plane of the tube, two branches and annulus. The adiabatic condition is applied to the surfaces of the upstream and downstream extensions, and the outside surfaces of the annulus and its two branches. The adiabatic condition is imposed on the outside surfaces of the annulus and branches, a uniform velocity, temperature and 5% turbulence intensity of water at the inlet of one branch, and the zero pressure are implemented at the outlet of the other branch, respectively. The pressure and temperature of water at the inlet, 5% turbulence intensity and $u_1=u_2=0$, $u_3=-0.1\text{m/s}$ constant velocities are given to the water fluid domain.

In the sole tube model, the boundary conditions at the inlet and outlet of the inner tube and on the surfaces of the upstream and downstream extensions are the same as those in the complete model. However, a known outward heat flux (negative value) is prescribed at the wall of the inner tube inside the HX. The pressure and temperature of SCO₂ at the inlet, 5% turbulence intensity and $u_1=u_2=0$, $u_3=1\text{m/s}$ constant velocities are assigned to the SCO₂ fluid domain.

2.4 Examination on mesh size independence

A mesh size independence examination was exercised with the sole tube model for the case: $p_1=8\text{MPa}$, $G=200\text{kg/m}^2\text{s}$, $q_w=12\text{kW/m}^2$, and $T_1=26-65^\circ\text{C}$. Three meshes, namely Mesh1, Mesh2 and Mesh3 were generated with three mesh sizes in the ANSYS meshing module, and their information is tabulated in Table 1. The pattern of these meshes is identical to the pattern

in the inner tube shown in Figure 7a. Six-node wedge elements (57-75%) are dominant over four-node tetrahedron elements. y^+ varies with mesh size and SCO₂ mean bulk temperature T_b , which is the mean temperature based on the local temperatures at ten axial locations shown in **Error! Reference source not found.** For Mesh1, Mesh2 and Mesh3, y^+ is in the ranges of 0.83-2.83, 0.86-2.67 and 0.73-2.19, respectively.

Table 1 The information about the meshes employed in CFD simulations of SCO₂

Geometrical model		Sole tube model			Complete model
Mesh name		Mesh1	Mesh2	Mesh3	Mesh 4
Element size(mm)		0.45	0.4	0.375	0.5
Nodes		469,305	773,564	1,089,292	936,709
Elements	Total	1,154,802	1,812,034	2,452,971	2,168,679
	Hex8	0(0%)	0(0%)	0(0%)	57,112(3%)
	Tet4	450,262(39%)	565,474(31%)	615,171(25%)	875,787(40%)
	Wed6	704,540(61%)	1,246,560(69%)	1,837,800(75%)	1,235,780(57%)
Element quality		0.3564±0.3790	0.3244±0.3457	0.3113±0.3171	0.4468±0.3505
Aspect ratio		26.55±26.07	22.73±23.46	23.33±26.33	15.62±22.64
Skewness		0.1420±0.1286	0.1147±0.1205	0.1086±0.1164	0.1420±0.1272
Orthogonal quality		0.8540±0.1270	0.8828±0.1198	0.8906±0.1162	0.8583±0.1274
Inflation mesh for boundary layer	First layer height(mm)	0.0055	0.005	0.004	0.0055
	Number of layers	10	14	18	16
	Growth rate	1.2	1.2	1.2	1.2
y^+	$G=200\text{kg/m}^2\text{s}$ $q_w=12\text{kW/m}^2$ $p_1=8\text{MPa}$ $T_1=26-65^\circ\text{C}$	0.83-2.83	0.86-2.67	0.73-2.19	1.03-2.90
Hex8-eight-node hexahedron element, Tet4-four-node tetrahedron element, We6-six-node wedge element, $y^+=\sqrt{\tau_w/\rho} y/\nu$, where τ_w is the shear stress at the wall, y is the distance to the nearest wall from the first mesh layer and ν is the local kinematic viscosity of SCO ₂ ; y^+ rises with increasing T_1 because of decreased ν .					

The MHTCs between the SCO₂ and the inner tube wall predicted with Mesh1, Mesh2 and Mesh3, are indicated in Figure 2a as a function of T_b . The MHTC is calculated by using a known wall heat flux q_w , mean wall temperature T_w , which is the mean of temperature at ten axial locations shown in Figure A.1, and SCO₂ mean bulk temperature T_b in terms of the following expression:

$$U = \frac{q_w}{T_b - T_w} \quad (1)$$

In Figure 2a, the pseudocritical point of SCO₂ at 8MPa occurs at $T_c=34.5^\circ\text{C}$ [15]. Both the predicted and measured MHTCs are in the maximum values at 35.1°C , which is slightly higher than the pseudocritical point T_c , then reduce precipitously away from that point, especially in the range $T_b < T_c$. Additionally, the coefficients vary considerably in the $T_b < T_c$ range with mesh size.

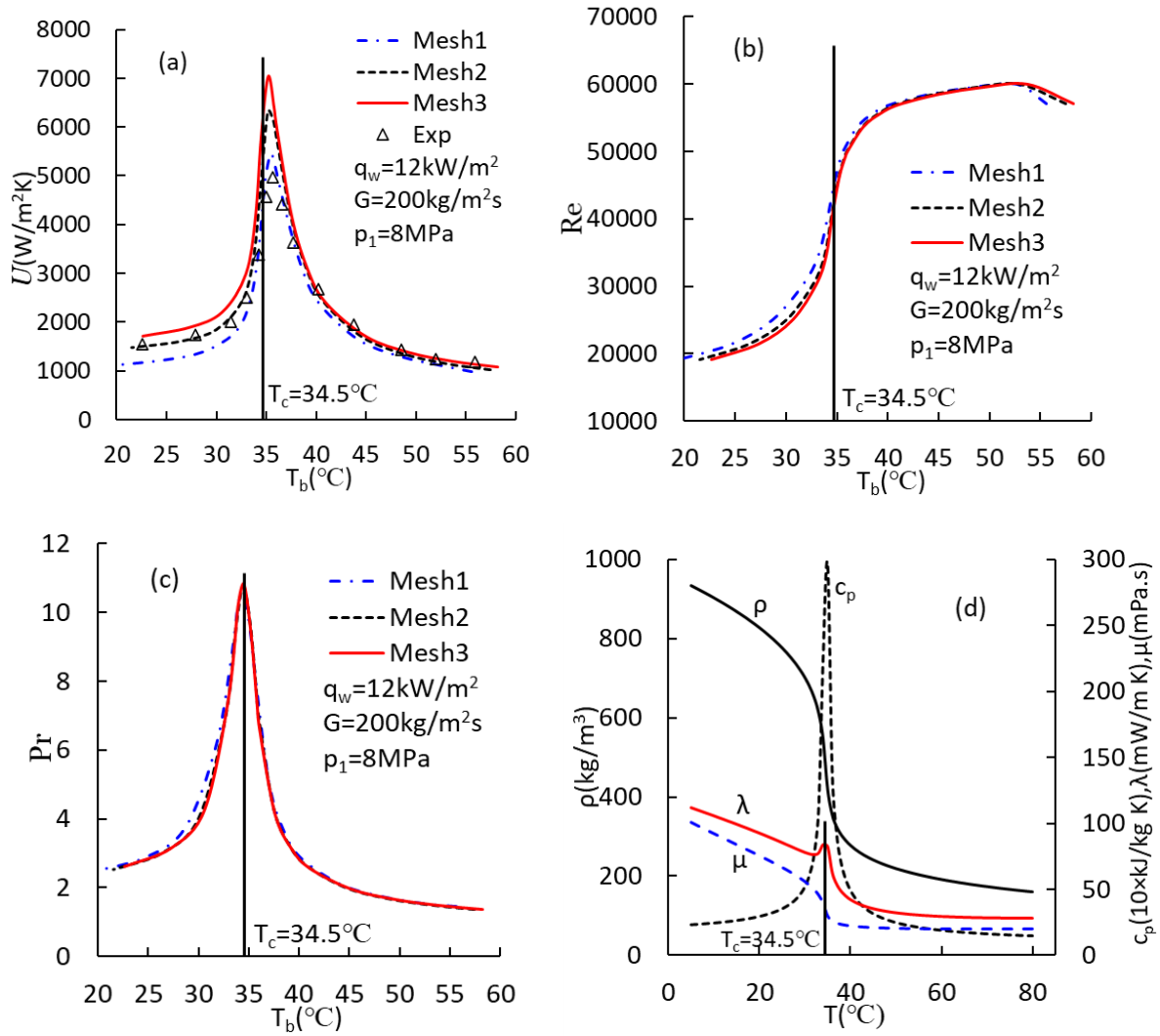


Figure 2 The SCO2 MHTCs and other parameters in the sole tube model in three meshes, Experimental data from [15], (a) MHTCs, (b) Reynolds number, (c) mean Prandtl number, (d) SCO2 thermophysical and transport properties

The relationship of the Reynolds number at the inner tube inlet with SCO2 mean bulk temperature is plotted in Figure 2b. The Reynolds number varies more significantly with mesh size on the left-hand side of the pseudocritical point than on the right-hand side of the point. This may be attributed to the sharp increase in the SCO2 dynamic viscosity, thermal conductivity and density with decreasing temperature as shown in Figure 2d.

Likewise, the predicted mean Prandtl number with Mesh1, Mesh2 and Mesh3 agrees well with each other except on the left-hand side of the pseudocritical point. Further, the maximum predicted Prandtl number emerges at $T_c=34.5^\circ\text{C}$ for all three meshes.

Based on Figure 2a, the MHTCs predicted with three meshes all agree with the experimental data [15] on the right-hand side of the pseudocritical point, but the MHTC in

Mesh2 agrees better with the measurement in comparison with those in Mesh1 and Mesh3. Thus, Mesh2 is adopted in CFD heat transfer simulations in the present study.

In Mesh2, the peak MHTC is 4.26 times larger than the MHTC at $T_b=26^\circ$. Based on the mean Prandtl number, which is the ratio of momentum diffusivity (kinematic viscosity) to thermal diffusivity of SCO_2 , shown in Figure 2c, the peak Prandtl number is 4.32 times higher than the number at $T_b=26^\circ$. Hence, the peak MHTC is caused by the peak Prandtl number. In the experiment [15], the ratio of the peak MHTC to the MHTC at $T_b=26^\circ$ is about 3.0. This value is smaller than the theoretical value of 4.26.

3 Results

3.1 Effects of turbulence model

The Wilcox $k-\omega$ and standard $k-\varepsilon$ two-equation turbulence models in 3D RANS methods are often applied in simulations of SCO_2 convective heat transfer [3] [13] [14], thus they were examined at two mass fluxes. The scalable log-law wall function [16] was used to the $k-\varepsilon$ two-equation model but the Automatic Near-Wall Treatment expressed by Eqs. (B.12) and (B.13) is adopted in the Wilcox $k-\omega$ model. In Mesh2, the two turbulence models were employed under the same flow conditions, the predicted SCO_2 MHTCs are plotted as a function of the SCO_2 mean bulk temperature in Figure 3. The errors in MHTC between the CFD prediction and the experimental data are tabulated in Table 2. The SST model results in the smallest error in the MHTC among the three turbulence models.

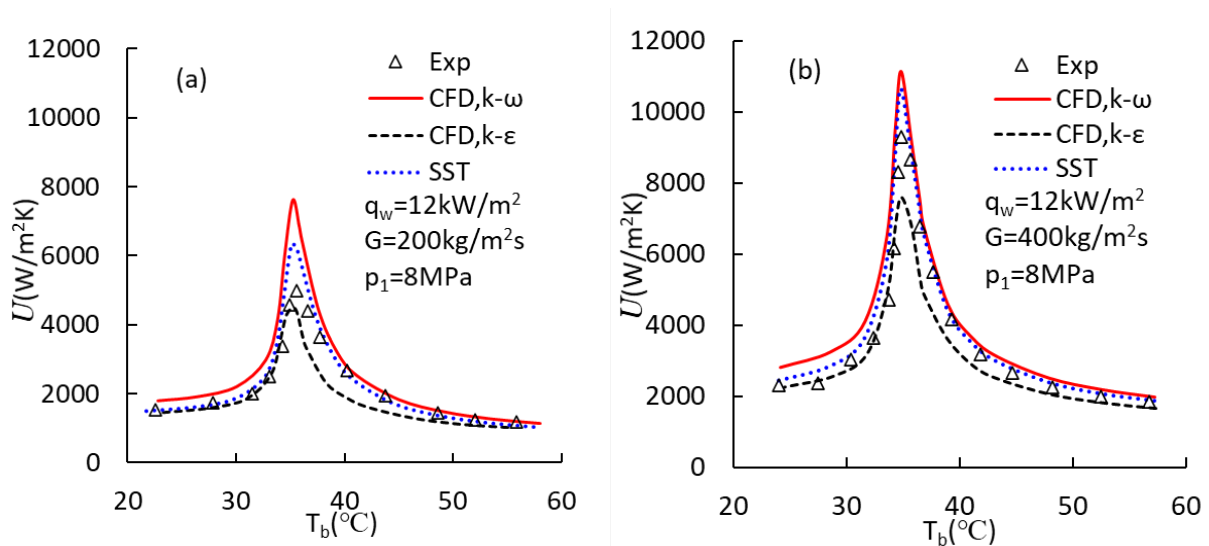


Figure 3 The SCO_2 MHTCs predicted with SST, $k-\omega$ and $k-\varepsilon$ two-equation turbulence models at two mass fluxes $G=200, 400\text{kg/m}^2\text{s}$, (a) $G=200\text{kg/m}^2\text{s}$, (b) $G=400\text{kg/m}^2\text{s}$, Exp-the experimental data from [15]

Table 2 The errors of MHTC predicted with three turbulence models in CFD simulations against the experimental data

Inner diameter, d (mm)	Inlet pressure, p_1 (MPa)	Wall heat flux, q_w (kW/m ²)	Mass flux, G (kg/m ² s)	Model	Error in MHTC (%)			
					max	min	mean	std
6	8	12	200	$k-\omega$	61.9	1.4	22.2	20.0
				$k-\varepsilon$	11.9	-30.1	-12.6	12.4
				SST	33.6	-9.6	6.1	14.1
			400	$k-\omega$	53.8	0.7	18.0	14.9
				$k-\varepsilon$	9.9	-22.3	-9.9	9.0
				SST	36.6	-2.4	9.7	11.1
The error in MHTC is defined as $100 \times (\text{prediction} - \text{experiment}) / \text{experiment}$, max-maximum error, min-minimum error, mean-mean error, std-standard deviation of error.								

At two mass fluxes, the $k-\varepsilon$ model gives a fairly good prediction on the left-hand side of the pseudocritical point, but an underpredicted MHTC on the right-hand side of the point. Contrarily, the $k-\omega$ model provides a decent prediction of MHTC on the right-hand side of the point, but an overprediction on the left-hand side of the point. The $k-\omega$ model overpredicts the MHTC at the pseudocritical point but the $k-\varepsilon$ model underestimates it. Obviously, the $k-\omega$ model is more suitable to SCO₂ flows at large mass flux and high inlet temperature, i.e., high Reynolds number, while the $k-\varepsilon$ model is more applicable to SCO₂ flows at small mass flux and low inlet temperature, i.e., low Reynolds number. In comparison with the $k-\omega$ and $k-\varepsilon$ models, the SST model produces even better MHTCs against the measurements at both mass fluxes.

Additional four turbulence models, including the eddy transport, renormalisation group (RNG) $k-\varepsilon$, baseline (BSL) $k-\omega$, and ω -stress models, which are not popular as the $k-\varepsilon$, $k-\omega$ and SST models, were attempted to simulate the SCO₂ convective heat transfer only in three inlet temperatures herein. The MHTCs predicted with these models are listed in Table 3 at 42.5 (right of T_c), 36 (near T_c) and 30°C (left of T_c) inlet temperatures, respectively. The results given by the standard $k-\varepsilon$, Wilcox $k-\omega$ and SST models are presented in the table, too. It is demonstrated that the MHTCs predicted by the eddy transport, standard $k-\varepsilon$ and RNG $k-\varepsilon$ models are very similar in the same inlet temperature and mass flux, and the MHTC produced by the RNG $k-\varepsilon$ model is the lowest in the three models.

Table 3 The MHTCs predicted with seven turbulence models at 42.5, 36 and 30°C inlet temperatures

Model		Eddy transport	$k-\varepsilon$		Wilcox $k-\omega$	Blended $k-\omega$ and $k-\varepsilon$		ω -stress
			Standard	RNG		BSL	SST	
Wall function		Scalable log-law			Automatic near Wall Treatment (blended linear-law and log-law)			
U (W/m ² K)	Right of T_c - 42.5°C	1936.7	1895.1	1721.2	3211.1	3224.1	3062.0	3361.3
	Near T_c - 36°C	4366.8	4464.3	3907.5	7604.6	7556.7	6319.1	8589.8
	Left of T_c - 30°C	1499.3	1604.1	1411.9	1915.7	1933.3	1609.9	2375.8

Likewise, the MHTCs estimated by the Wilcox $k-\omega$, BSL $k-\omega$, SST and ω -stress models are close to each other in magnitude in the same inlet temperature and mass flux. Particularly, the MHTCs predicted by the SST model are the smallest among these four models. This effect possibly could be attributed to the eddy viscosity suppressed by Eq. (20). Based on Figure 3, the MHTCs produced by the SST model are the closest to the experimental observations, thereby, the SST model should be adopted in SCO₂ heat transfer simulations.

3.2 Effects of inlet pressure

Since the thermophysical and transport properties of SCO₂ relate to both temperature and pressure, e.g., specific heat capacity at constant pressure C_p , as shown in Figure 4a, the inlet pressure can affect MHTC in the tube-in-tube HX. The effect of SCO₂ inlet pressure on the MHTC is demonstrated in Figure 4b under the condition of $G=400\text{kg/m}^2\text{s}$, $q_w=12\text{kW/m}^2$ and $d=6\text{mm}$ tube inner diameter. Because the pseudocritical point moves to a higher temperature and the corresponding specific heat capacity decreases as the inlet pressure increases, the Λ -shaped MHTC curve moves to a higher temperature range and becomes blunter with the increasing inlet pressure. The predicted MHTC curves agree well with the experimental data and reflect their variation with inlet pressure precisely. For instance, the maximum, minimum, mean, and standard deviation of the error in MHTC against the experimental data are 12.2%, -13.6%, 0.6% and 7.3% at $p_1=9\text{MPa}$, compared with 36.6%, -2.4%, 9.7% and 11.1% at $p_1=8\text{MPa}$.

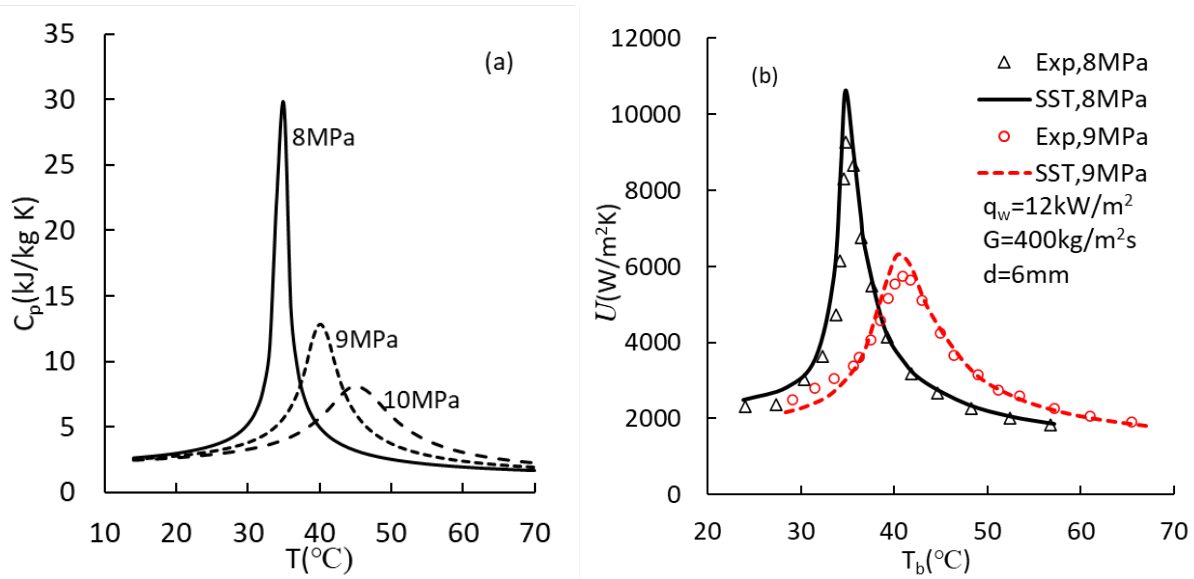


Figure 4 The MHTCs of SCO_2 at the inlet pressures of 8 and 9 MPa, respectively, but the SCO_2 mass flux $G=400 \text{ kg/m}^2\text{s}$, wall heat flux $q_w=12 \text{ kW/m}^2$, and tube diameter $d=6 \text{ mm}$ remain unchanged, (a) SCO_2 specific heat capacity-temperature curves at constant pressure, (b) SCO_2 MHTC-mean bulk temperature curve, the experimental data after [15]

At the pseudocritical points, the heat capacity is decreased by 56.6% when the inlet pressure increases from 8 MPa to 9 MPa. Comparably, the peak MHTC decreases by 40.5% in the CFD simulation, and 38.2% in the experiment. This fact suggests that the specific heat capacity is responsible for the Λ -shaped MHTC curve and its varying trend with the mean bulk temperature of SCO_2 .

3.3 Effects of mass flux and wall heat flux

The effect of SCO_2 mass flux on MHTC is demonstrated in Figure 5a. If the tube diameter, inlet pressure and inlet temperature are given, then the Reynolds number of SCO_2 ascends or descends as the mass flux of SCO_2 increases or decreases. Usually, the heat transfer coefficient will rise or decline with increased or decreased Reynolds number. As a result, the MHTC should rise or decline with increased or decreased mass flux. This trend is clearly indicated in the figure.

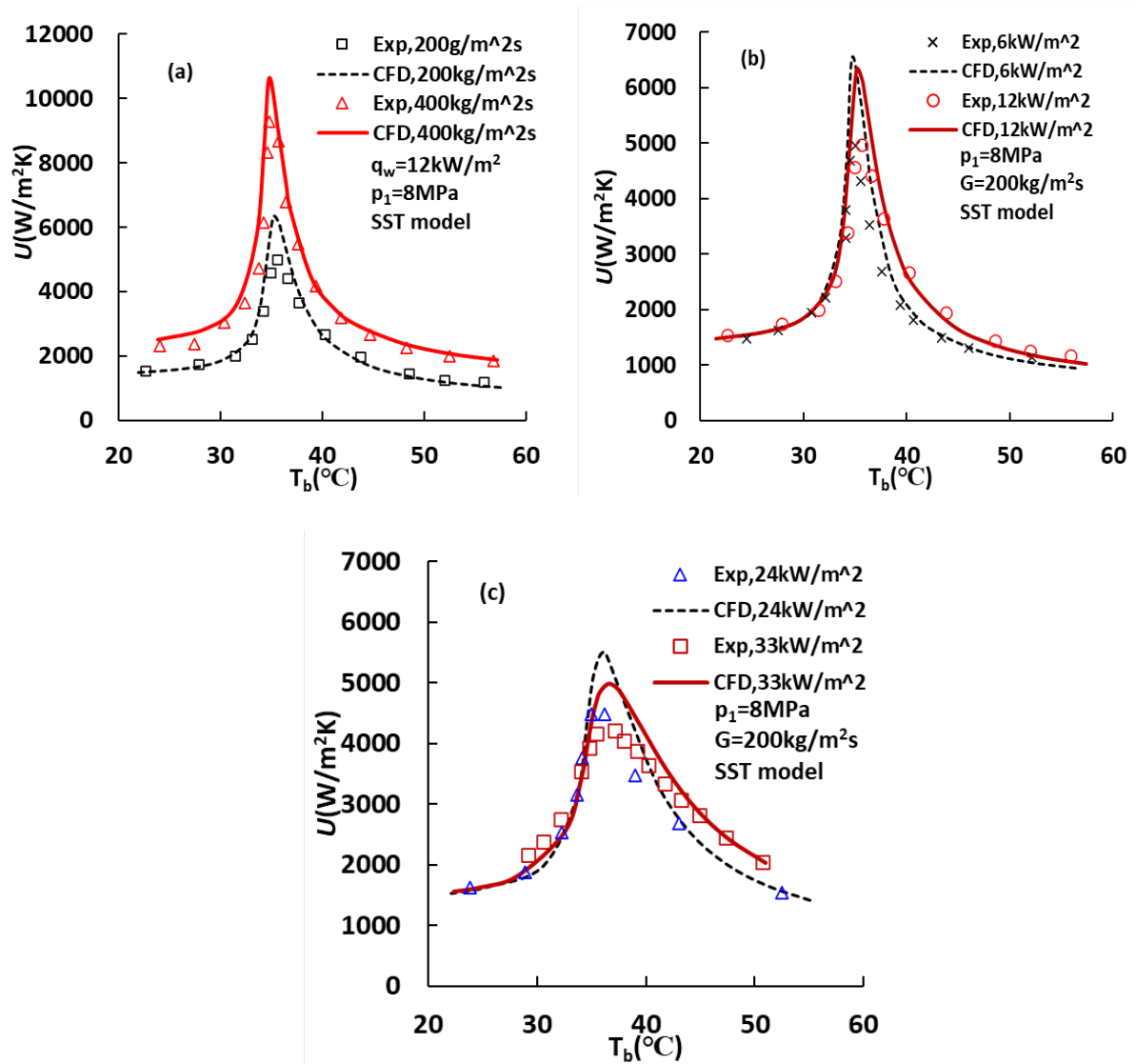


Figure 5 The effects of mass flux and wall heat flux on SCO₂ MHTC, (a) the effect of mass flux, (b) and (c) wall heat flux, the experimental data after [15]

The effect of wall heat flux on SCO₂ MHTC is presented in Figure 5b and c at a given SCO₂ mass flux of $G=200$ kg/m²s. The wall heat flux is primarily determined by the temperature difference across the inner tube wall. The SCO₂ MHTC is in a Λ -shaped curve at the wall heat fluxes of 6, 12, 24 and 33 kW/m² against the mean bulk temperature. However, the peak coefficient declines, and two legs rise with increasing wall heat flux. Both the predicted and the measured MHTCs reflect this property. The errors of the MHTC predicted against the experimental data are listed in Table 4. The agreement in the MHTCs between prediction and measurement is quite good when the wall heat fluxes are at 12, 24 and 33 kW/m². The largest error in the MHTC is found at and near the pseudocritical point at the wall heat flux of 6 kW/m².

Table 4 The errors of MHTC between CFD prediction and experimental data under various conditions

HX model	d (mm)	p_1 (MPa)	G (kg/m ² s)	q_w (kW/m ²)	Order of advection scheme	Option in CFX-Post	Buoyancy	Error in MHTC (%)			
								max	min	mean	std
Sole tube	6	9	400	12	1 st	Con	No	12.2	-13.6	0.6	7.3
	6	8	200	6	1 st	Con	No	35.5	-8.6	13.4	14.1
				12	1 st	Con	No	33.6	-9.6	6.1	14.1
				24	1 st	Con	No	22.9	-11.5	4.0	10.6
				33	1 st	Con	No	17.8	-13.9	3.7	10.3
	1 st	Hybrid	No		4.4	-32.0	-9.7	13.6			
	2 nd	Hybrid	No		24.9	-12.3	6.7	11.8			
	1 st	Con	Yes		50.6	-3.8	24.0	17.0			
	1 st	Hybrid	Yes	11.7	-15.7	0.5	8.2				
	4	9	600	12	1 st	Con	No	12.6	-8.1	3.1	7.2
Complete	6	8	200	12	1 st	Con	No	53.0	-1.8	18.0	16.9

The error in MHTC is defined as (prediction-experiment)×100%/experiment, Con-conservative value in CFX-Post, hybrid-hybrid values in CFX-Post, max-maximum error, min-minimum error, mean-mean error, std-standard deviation of error, the order of advection scheme is for the advection terms in the equations of the SST model.

3.4 Effects of tube inner diameter

Usually, the MHTC at the wall in a tube with a small inner diameter is higher than in a tube with a big inner diameter at the same Reynolds number. The Reynolds number of SCO₂ flowing in a tube is defined as

$$Re_b = \frac{u_b d \rho_b}{\mu_b}, \quad u_b = \frac{G \frac{\pi}{4} d^2}{\rho_b \frac{\pi}{4} d^2} = \frac{G}{\rho_b} \quad (2)$$

where ρ_b is the bulk density of SCO₂, μ_b is the bulk dynamic viscosity of SCO₂, u_b is the bulk velocity of SCO₂ in the tube. Based on mass flux G and viscosity μ_b , SCO₂ Reynolds number in a tube is expressed by

$$Re_b = \frac{Gd}{\mu_b} \quad (3)$$

The MHTCs in the tubes with 4mm and 6mm inner diameters are plotted as a function of SCO₂ mean bulk temperature in Figure 6. In the figure, Gd is identical for the two tubes, as a result, at the same fluid mean bulk temperature, the fluids in the two tubes have an identical Reynolds number. Clearly, the MHTC in the tube with a small diameter is higher than in the tube with a big diameter at the same mean bulk temperature. The trend of the predicted MHTC agrees well with the experimental data, see Table 4 for the errors.

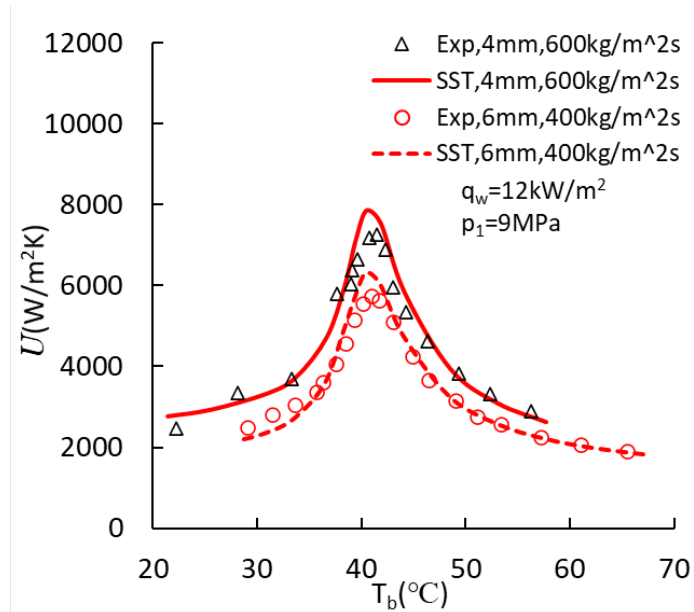


Figure 6 The MHTCs in two tubes with 4mm and 6mm inner diameters are plotted as a function of SCO2 mean bulk temperature, symbol-experimental data in [15], line-CFD prediction

3.5 Effects of geometrical model

Initially, CFD heat transfer simulations were performed on the complete geometrical model as shown in Figure 1a. In a simulation, besides the SCO2 mass flux, inlet pressure and temperature, the inlet temperature and flow rate of the cooling water must be provided to meet a known experimental wall heat flux between the SCO2 and the cooling water. Since there is no information about the inlet temperature and flow rate of the cooling water in [15], it is extremely hard and time-consuming to provide the correct inlet temperature and flow rate of the cooling water for a known wall heat flux in [15] so as to match the experimental MHTCs. Therefore, just one case was performed successfully, and the corresponding MHTCs are illustrated in Figure 7, where the partial view of the mesh is shown, too. The information on the mesh (i.e., Mesh4) is listed in Table 1. Since the y^+ values are comparable to the Mesh2, a check on mesh size independence is not exercised.

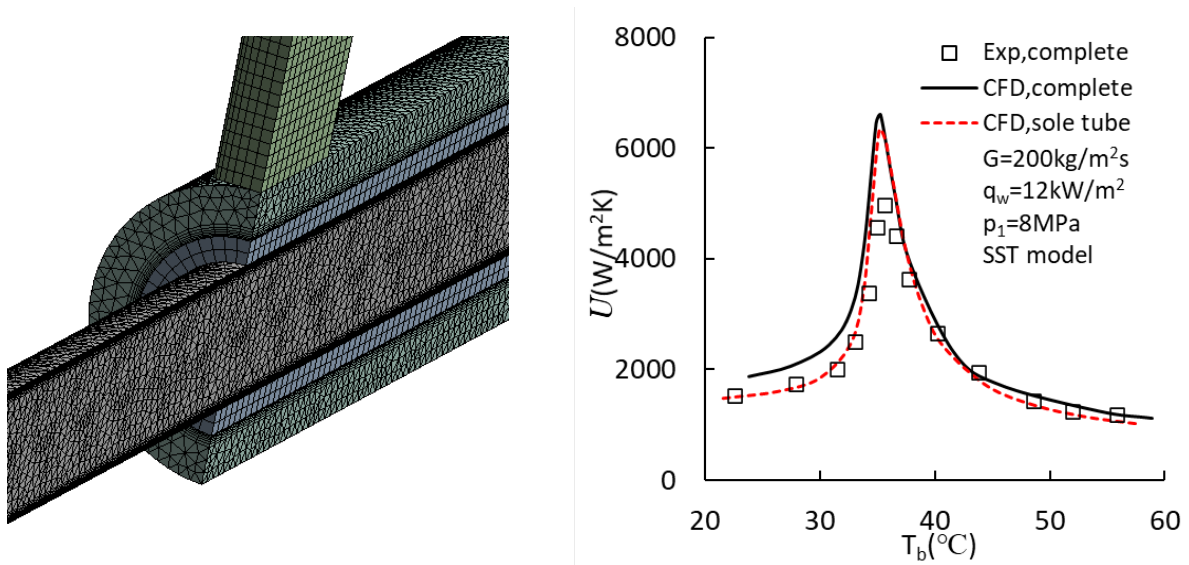


Figure 7 The effect of complete geometrical model and sole tube geometrical model on SCO2 MHTC, the experimental data after [15]

In comparison with the MHTC from the sole tube geometrical model, the MHTC based on the complete geometrical model agrees well with the experimental data on the right-hand side of the pseudocritical point, but poorly on the left-hand side of the point. As shown in Table 4, even though the minimum error of MHTC against the experimental data is quite small (-1.8%), the maximum and mean errors are as large as 53.0% and 18.0%, respectively. This suggests that the guessed water flow rate and inlet temperature which have met the experimental wall heat flux may not be those experienced in the experiment. For this reason, the complete geometrical model has to be abandoned.

The temperature contours of the SCO2 flow in the two geometrical models are demonstrated in Figure 8 under the same thermal and flow conditions: $G=200kg/m^2s$, $q_w=12kW/m^2$, $p_1=8MPa$ and $T_1=30, 65^{\circ}C$. The SCO2 temperature contours in the complete model are remarkably similar to those in the sole tube model in the same inlet temperature, pressure and mass flux. However, the profile of the core hot flow in the former is longer and narrower than in the latter model, especially at $T_1=30^{\circ}C$. This might be caused by the lower inlet temperature of water assumed.

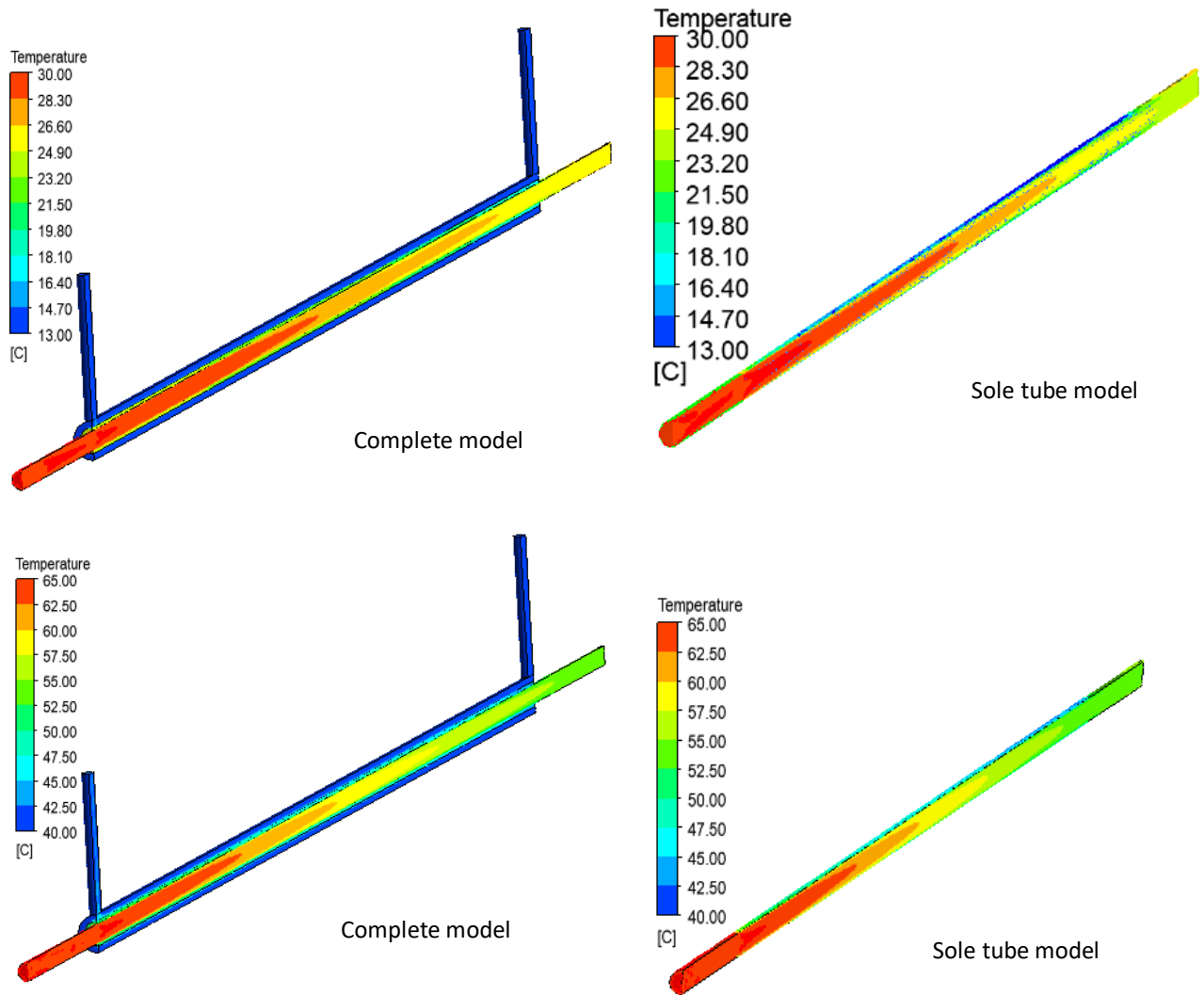


Figure 8 The temperature contours of the SCO₂ flow predicted based on the complete geometrical and sole tube models at the same SCO₂ thermal and flow conditions: $G=200\text{kg/m}^2\text{s}$, $q_w=12\text{kW/m}^2$, $p_1=8\text{MPa}$, $T_1=30, 65^\circ\text{C}$

4 Discussion

A series of CFD simulations of convective heat transfer in the experimental counter-flow tube-in-tube HX in [15] was performed when SCO₂ was cooled by a stream of water. First, the most suitable turbulence model and mesh size were identified. The influences of SCO₂ inlet pressure, mass flux, wall heat flux and geometrical model of the HX on the MHTC curve were then examined and compared with the experimental data of the MHTC in [15]. These comparisons are more extensive and complete than those in the literature. Similar work has not been seen in the literature as well.

Frankly, a couple of issues, such as mesh size independence, numerical scheme, CFD result extraction method and buoyancy effect are important to SCO₂ convective heat transfer

simulations, and there are a few limitations in the paper. These issues will be discussed in the following sections.

4.1 An explanation of mesh size independence

In Section 2.4 the mesh size independence is achieved on the right-hand side of the pseudocritical point, and the MHTC still varies with the mean bulk temperature on the left-hand side of the point and at the point itself. This phenomenon will be explained here. The MHTC is associated with the heat transfer coefficient in the laminar/viscous sublayer at the wall. Eq. (B.13) was employed in CFX to model the heat transfer in the viscous sublayer analytically. Based on the equation the heat transfer coefficient $q_w/(T_w - T_n)$ across the layer is expressed as

$$\begin{cases} \frac{q_w}{T_w - T_n} = \frac{\rho C_p u_\tau}{T^+}, T^+ = Pr y^+ e^{-\Gamma} + [0.1 \ln(y^+) + \beta] e^{-1/\Gamma}, \Gamma = \frac{0.01(Pr y^+)^4}{1 + 5Pr^3 y^+} \\ Pr = \frac{\mu C_p}{\lambda}, \beta = (3.85 Pr^{1/3} - 1.3) + 0.1 \ln(Pr) \end{cases} \quad (4)$$

where the Prandtl number Pr , the density ρ , specific heat capacity at constant pressure C_p and wall shear stress τ_w of SCO₂ are extracted from a CFD result simulated, the dimensionless velocity in the viscous sublayer u_τ is equal to $\sqrt{\tau_w/\rho}$, i.e., $u_\tau = \sqrt{\tau_w/\rho}$ yields. The heat transfer coefficient $q_w/(T_w - T_n)$ at three typical inlet temperatures $T_1 = 26, 36, 65^\circ\text{C}$, and the inlet pressure $p_1 = 8\text{MPa}$, mass flux $G = 200\text{kg/m}^2\text{s}$, wall heat flux $q_w = 12\text{kW/m}^2$ were calculated with Eq. (4), and plotted in Figure 9 after being normalized with the maximum $q_w/(T_w - T_n)$ values based on $u_\tau = 1.78, 2.89, 5.25\text{cm/s}$, $Pr = 2.60, 10.8, 1.36$, $C_p = 3211.8, 23995, 2069.8\text{J/kg K}$.

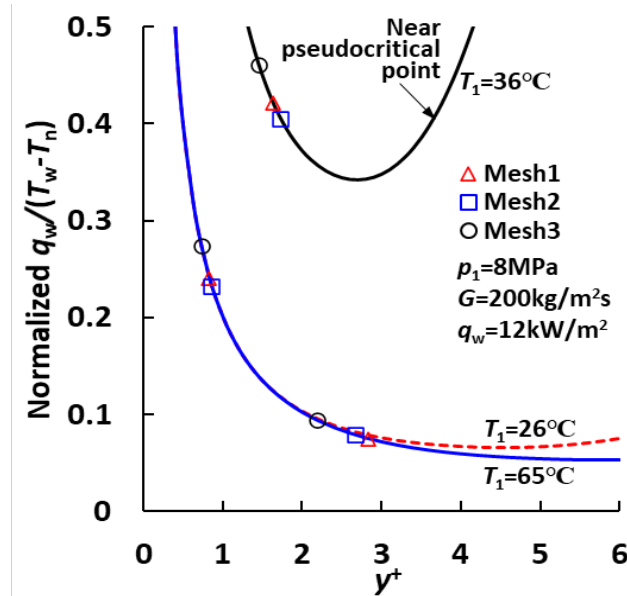


Figure 9 The normalized heat transfer coefficient across the viscous sublayer versus y^+ under the conditions: $T_1 = 26, 36, 65^\circ\text{C}$, $p_1 = 8\text{MPa}$, $G = 200\text{kg/m}^2\text{s}$, and $q_w = 12\text{kW/m}^2$

The shape of the normalized $q_w/(T_w - T_n)$ curve at $T_1=26^\circ\text{C}$ is similar to that at $T_1=65^\circ\text{C}$, but different from that at $T_1=36^\circ\text{C}$. The change in mesh size can result in a variation in normalized $q_w/(T_w - T_n)$ on the curve. Obviously, when the mesh size changes from Mesh1 to Mesh3, the largest variation in the normalized $q_w/(T_w - T_n)$ is found at $T_1=36^\circ\text{C}$, the moderate variation occurs at $T_1=26^\circ\text{C}$, while the smallest variation is observed at $T_1=65^\circ\text{C}$. This variation trend of the normalized $q_w/(T_w - T_n)$ seems to be responsible for the MHTC curves in Mesh1, Mesh2 and Mesh3 shown in Figure 2a.

Additionally, the y^+ values in the three meshes at $T_1=26, 36^\circ\text{C}$ are in the regions with a steeper slope in the normalized $q_w/(T_w - T_n)$ curves. However, the y^+ values in the meshes at $T_1=65^\circ\text{C}$ are located in the range with a flatter slope. The mesh size at $T_1=26, 36^\circ\text{C}$ should be altered to allow the corresponding y^+ values to be moved into a region with a smaller slope in the normalized $q_w/(T_w - T_n)$ curves. In this case, the mesh size independence will reach on the left-hand side of the pseudocritical point and the point itself. This fact suggests that the different mesh sizes should be adopted for the different inlet temperatures in SCO₂ heat transfer simulations. Note that the mesh size independence was explored and achieved at the single inlet temperature of 330K ($\approx 57^\circ\text{C}$) in terms of local heat transfer coefficient in [3] rather than in a range of inlet temperatures in terms of MHTC in the present paper.

4.2 The maximum MHTC point

The maximum MHTC of SCO₂ occurs at a higher mean bulk temperature than the pseudocritical point, as shown in Figure 2a for the given inlet pressure of 8MPa. This phenomenon has been observed when SCO₂ was cooled in a tube-in-tube HX [18]. The reason for this effect is attributed to uneven temperature profile in a cross-section of the tube and the wall temperature is the lowest in the cross-section [18]. The CFD simulations do prove that the uneven temperature profile exists, see Figure 8. As the pressure rises, the SCO₂ specific heat capacity at the pseudocritical point is not much larger than those at the other temperatures, as illustrated in Figure 4a, therefore, this phenomenon is less dominant when the inlet pressure is higher than 8MPa.

4.3 Effect of conservative and hybrid values of wall temperature

The MHTC of SCO₂ has been overpredicted at the pseudocritical point and in its nearby regions, as shown in Figure 2 to Figure 7. The same phenomenon has been observed in the MHTC predicted with the SST model [6] [7] [8] [9] [10]. This might be resulted from the difference between the mean temperature at the tube wall and the mean bulk temperature of SCO₂. Fluid flow variables such as velocity, temperature, pressure, and density are defined and solved in control volumes in the ANSYS CFX solver. As default, i.e., **conservative option** in CFX-Post, a flow variable at a mesh node at the wall is calculated by averaging the variable in its surrounding control volumes without any interpolation from the variables in

internal control volumes to that at a node on the boundary. The velocity calculated in this way is non-zero for the no-slip velocity boundary. Fortunately, the **hybrid option** is provided in CFX-Post, where the variable is interpolated from the variables in internal control volumes, and the velocity at a wall keeps zero for the no-slip velocity condition.

The MHTC shown in the foregoing figures (Figure 2-Figure 7) is based on the mean wall temperature calculated with the **conservative option**, which is called the conservation value. For comparison, the MHTC calculated with the **hybrid option**, which is known as the hybrid value, is illustrated in Figure 10 with two cases: (1) $q_w=12\text{kW/m}^2$, (2) $q_w=33\text{kW/m}^2$, while $G=200\text{kg/m}^2\text{s}$, $d=6\text{mm}$, and $p_1=8\text{MPa}$ remain unchanged. The MHTC, i.e., U , is calculated with known wall heat flux q_w and the difference in the mean temperature T_b-T_w by using Eq. (1). Note that T_b and T_w are obtained from CFD simulations, but only the values of T_w depend on the **hybrid** or **conservative option**.

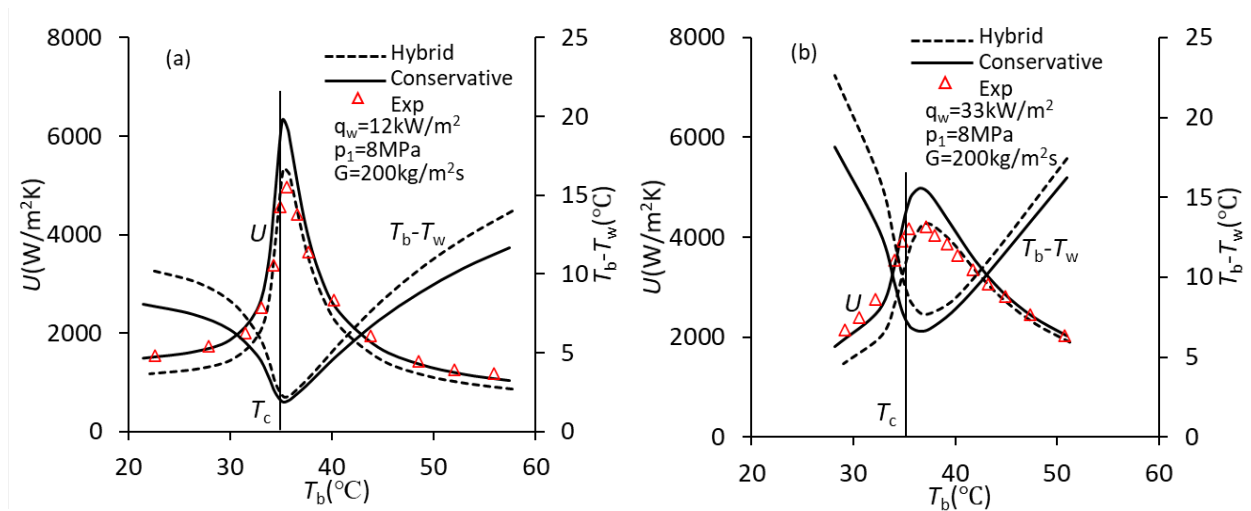


Figure 10 The effects of hybrid and conservative options on the MHTC in two cases in 6mm tube diameter, the experimental data after [15]

Since q_w is constant in each case, the U is proportional to the mean temperature difference ($T_b - T_w$) inversely. The values of ($T_b - T_w$) are minimum when the **conservative option** is held somewhere near the pseudocritical point. Therefore, a small change in ($T_b - T_w$) can result in a significant increase in U there. This effect should be responsible for the overprediction in U . The overprediction disappears when the **hybrid option** is chosen due to the raised ($T_b - T_w$). However, the U curve moves down, and a significant error in the U occurs on the left-hand side of the pseudocritical point.

4.4 Effect of advection scheme in SST model

The numerical discretisation scheme of the advection terms in the SST model influences the MHTC of SCO_2 significantly. In ANSYS CFX, two discretisation schemes are

provided: one is 2nd-order high-resolution scheme, and the other is 1st-order upwind scheme. The high-resolution (2nd-order) scheme was imposed on the advection terms in RANS equations. However, the high-resolution scheme and the 1st-order scheme have been tried for the advection terms in the SST model. The MHTCs predicted with the high-resolution scheme are illustrated in Figure 11 under the conditions: $p_1=8\text{MPa}$, $G=200\text{kg/m}^2\text{s}$ and $q_w=33\text{kg/m}^2$. The MHTC predicted with the 2nd-order scheme and the wall temperature of the hybrid values overlaps the coefficient predicted with the 1st-order scheme and the wall temperature of conservative values in the ranges $T_b<35^\circ\text{C}$ and $T_b>40^\circ\text{C}$. In the range near the pseudocritical point, however, the coefficient predicted with the 2nd-order scheme is above the coefficient predicted with the 1st-order scheme. The 2nd-order scheme intensifies the overprediction in the coefficient in the range near the point. The errors in the MHTC in Table 4 reflect this feature, too.

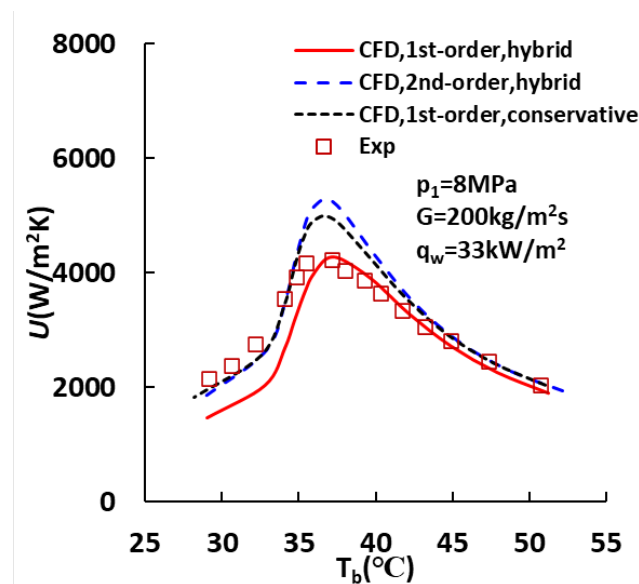


Figure 11 The comparison of the MHTCs predicted between 2nd-order (high resolution) and 1st-order schemes for the advection terms in the SST model under the conditions: $p_1=8\text{MPa}$, $G=200\text{kg/m}^2\text{s}$ and $q_w=33\text{kg/m}^2$, the experimental data from [15]

The predicted MHTCs with the two schemes are illustrated in Table 5 at $G=200\text{kg/m}^2\text{s}$, $p_1=8\text{MPa}$, $q_w=12\text{kg/m}^2$ and $T_i=42.5, 36, 30^\circ\text{C}$, respectively. The 2nd-order scheme can raise the MHTC by (11-28)%, dependent on the mean bulk temperature of SCO_2 , especially at the pseudocritical point and on the left-hand side of the Λ -shaped MHTC curve. As a result, it slightly improves the agreement between the prediction and the measurement on the left-hand side of the Λ -shaped curve but makes it worse on the right-hand side of the curve. The high-resolution scheme for the advection terms in the SST model can increase y^+ and wall shear stress values. In this regard, the 1st-order scheme for the advection terms in the SST model was adopted in CFD simulations of SCO_2 heat transfer here.

Table 5 The effect of discretisation scheme of advection terms in the SST model on MHTC at $G=200\text{kg/m}^2\text{s}$, $p_1=8\text{MPa}$, $q_w=12\text{kW/m}^2$ and $T_1=42.5, 36, 30^\circ\text{C}$

U (W/m ² K)	1 st -order	2 nd -order	Increment (%)
Right of T_c -42.5°C	2652.5	2952.0	11.3
Near T_c -36°C	5319.1	6779.7	27.5
Left of T_c -30°C	1268.2	1560.9	23.1

4.5 Buoyancy Effect

Like SCO₂ flowing in vertical miniature tubes [19] [14], mini or normal size tubes [18] [20] [21] [22], or an inclined tube [11] [23], there exists buoyancy effect that non-uniformity of SCO₂ density can significantly influence on the primary flow, turbulence fields, and heat transfer effectiveness in a horizontal tube [4] [24] when the SCO₂ is heated or cooled. The SCO₂ heat transfer in vertical tubes with buoyancy effect was modelled analytically [25] [26] and investigated numerically based on CFD [27] [28] [8] [9] [29]. The buoyancy effect can impair SCO₂ heat transfer effectiveness, resulting in heat transfer deterioration in all these arrangements except SCO₂ downward flows. The impaired heat transfer or heat transfer deterioration relates to suppressed or reduced turbulence production near the wall.

The Nusselt number of SCO₂ with buoyancy effect can be correlated to a buoyancy parameter Gr_b/Re_b^n , where Gr_b and Re_b are the Grashof number and Reynolds number of SCO₂ in a tube, n is a constant, depending on the tube orientation [30], and for a horizontal tube, $n=2$ [19], Gr_b/Re_b^2 called Richardson number Ri . When SCO₂ in a tube is cooled with a stream of water outside the tube, the Grashof number Gr_b is expressed as:

$$Gr_b = \frac{(\rho_w - \rho_b)\rho_b g d^3}{\mu_b^2} \quad (5)$$

where ρ_w is the density of SCO₂ at the tube wall, g is the acceleration of gravity, $g=9.81\text{m/s}^2$, u_b is calculated from SCO₂ mass flux and tube diameter with the following expression:

$$Ri = \frac{Gr_b}{Re_b^2} = \frac{(\rho_w - \rho_b)gd}{\rho_b u_b^2} \quad (6)$$

Replacing u_b in Eq.(6) with the expression in Eq.(2), Ri arrives at the following expression

$$Ri = \frac{(\rho_w - \rho_b)\rho_b g d}{G^2} \quad (7)$$

The Richardson number Ri relates explicitly to G , d , ρ_b and ρ_w . Specially, ρ_b and ρ_w depend on the inlet pressure and temperature of SCO₂, and wall heat flux. Usually, a large wall heat flux can lead to a significant difference $\rho_w - \rho_b$, and a low inlet temperature and a high inlet pressure will result in a large ρ_b . Thus, a large wall heat flux, low inlet temperature, high inlet pressure, big tube diameter and small mass flux will raise Ri value to intensify the

buoyancy effect on the heat transfer behaviour of SCO₂. The Ri of SCO₂ is plotted in Figure 12 as a function of SCO₂ mean bulk temperature T_b for four cases selected from Table A.1.

At the fixed d , p_i , G and q_w , the Ri of SCO₂ varies with mean bulk temperature T_b , and arrives at a peak near the pseudocritical point. At the same T_b , the Ri changes from one case to another but in the range of 0.0014-0.23. The heat transfer regime of SCO₂ in a cooled horizontal tube depends on the Richardson number. Theoretically, when $Ri < 0.001$, the natural heat transfer induced by the buoyancy effect can be negligible [19] and the SCO₂ heat transfer is purely forced convective heat transfer. When $Ri > 0.01$, the buoyancy effect will play a part in SCO₂ heat transfer in a cooled horizontal tube [3]. When $0.1 < Ri < 10$, the SCO₂ heat transfer in the tube is mixed convection of natural convection and forced convection [4] [5]. Based on these criteria for SCO₂ heat transfer in a cooled horizontal tube, the heat transfer in four cases shown in Figure 12 should be mixed convection and the buoyancy effect should be considered in CFD simulations of SCO₂ heat transfer.

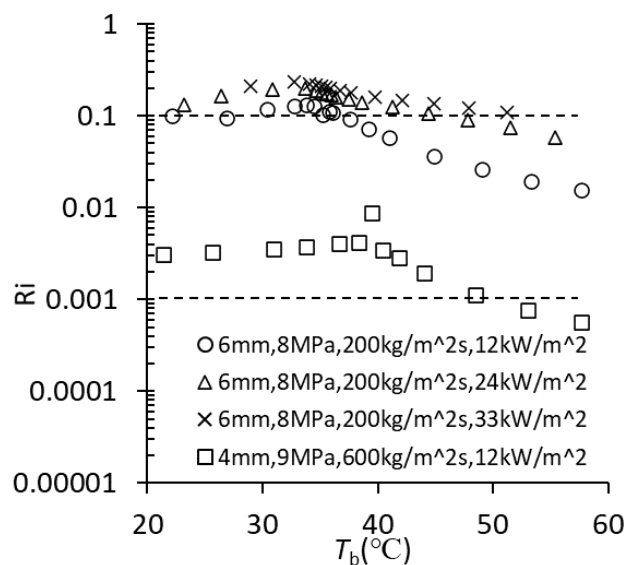


Figure 12 The Richardson number Ri is plotted as a function of SCO₂ mean bulk temperature T_b under different tube diameters, SCO₂ inlet pressures, mass fluxes and wall heat fluxes

Based on the figure, the buoyancy effect is the strongest in the case: $d=6\text{mm}$, $p_i=8\text{MPa}$, $G=200\text{kg/m}^2\text{s}$ and $q_w=33\text{kW/m}^2$. CFD Simulations of the case were launched when the buoyancy effect was taken into account and the predicted MHTC is shown in Figure 13a. The Boussinesq approximation was implemented, and the reference condition of the buoyancy effect is at the critical point. Thus, the SCO₂ density ρ and specific body force S_i in Eq.(11) are expressed as

$$\rho = \rho_0 - \beta_v \rho_0 (T - T_0), S_i = g_i \quad (8)$$

where ρ_0 and T_0 are the reference density and temperature of SCO₂ at the critical point, β_v is the volumetric thermal expansion coefficient of SCO₂, g_i are the components of the acceleration of gravity. Because the coordinate x_2 of the coordinate system of the flow domain is downward, see Figure 1, $g_1 = g_3 = 0$, $g_2 = 9.81 \text{ m/s}^2$ are held. Since the inlet temperature of SCO₂ is low in CFD simulations, the viscous dissipation has a negligible contribution to the buoyancy effect and the viscous dissipation to the effect was disabled.

In the figure, the buoyancy effect can raise the MHTC by using downward secondary flow near the tube wall. Additionally, when the wall temperature is calculated by means of conservative values, the MHTC increases significantly. Although the agreement between the prediction and the observation is improved on the left branch of the Λ -shaped curve, the agreement on the right-hand side is poorer. If the hybrid option is employed to calculate the wall temperature, the MHTC with buoyancy effect exhibits pretty good agreement with the experimental one, the corresponding errors are demonstrated in Table 4.

In Figure 13b, a secondary flow starts to be induced after the SCO₂ flows into the segment where there is an outward heat flux applied at the wall in the tube-in-tube HX. The SCO₂ fluid elements with a lighter density at the bottom stream upwards to near the central vertical plane until the top, then go down along the tube wall until the bottom to finish a cycle. Such a cycle is repeated until the SCO₂ is out of the segment. Since the SCO₂ fluid elements are carried by the primary flow downstream, the secondary flow moves in the tube in a spiral pattern. Since the secondary flow brings the core hot fluid to the wall and results in long flow paths, the SCO₂ heat transfer is enhanced. The well-known heat transfer deterioration does not exist in the horizontal tube-in-tube HX under SCO₂ flow conditions.

In Figure 13c, the temperature contour of SCO₂ in the cross-sections of the tube develops into nonuniform profiles gradually from the inlet to the outlet, and the low-temperature zone with increased size downstream is located in the region near the bottom of the tube, exhibiting a thermal stratification effect. As shown in Figure 13d, the low-velocity zone also accumulates in the area near the bottom of the tube and expands from the inlet to the outlet. Obviously, the temperature and velocity profiles are no longer symmetrical about the horizontal plane through the centre line of the tube due to the buoyancy effect. If the effect is not taken into account in the CFD simulation the temperature (Figure 8) or velocity will be symmetrical about the centre line. The flow patterns, velocity and temperature contours shown in Figure 13 are consistent with those presented in [5].

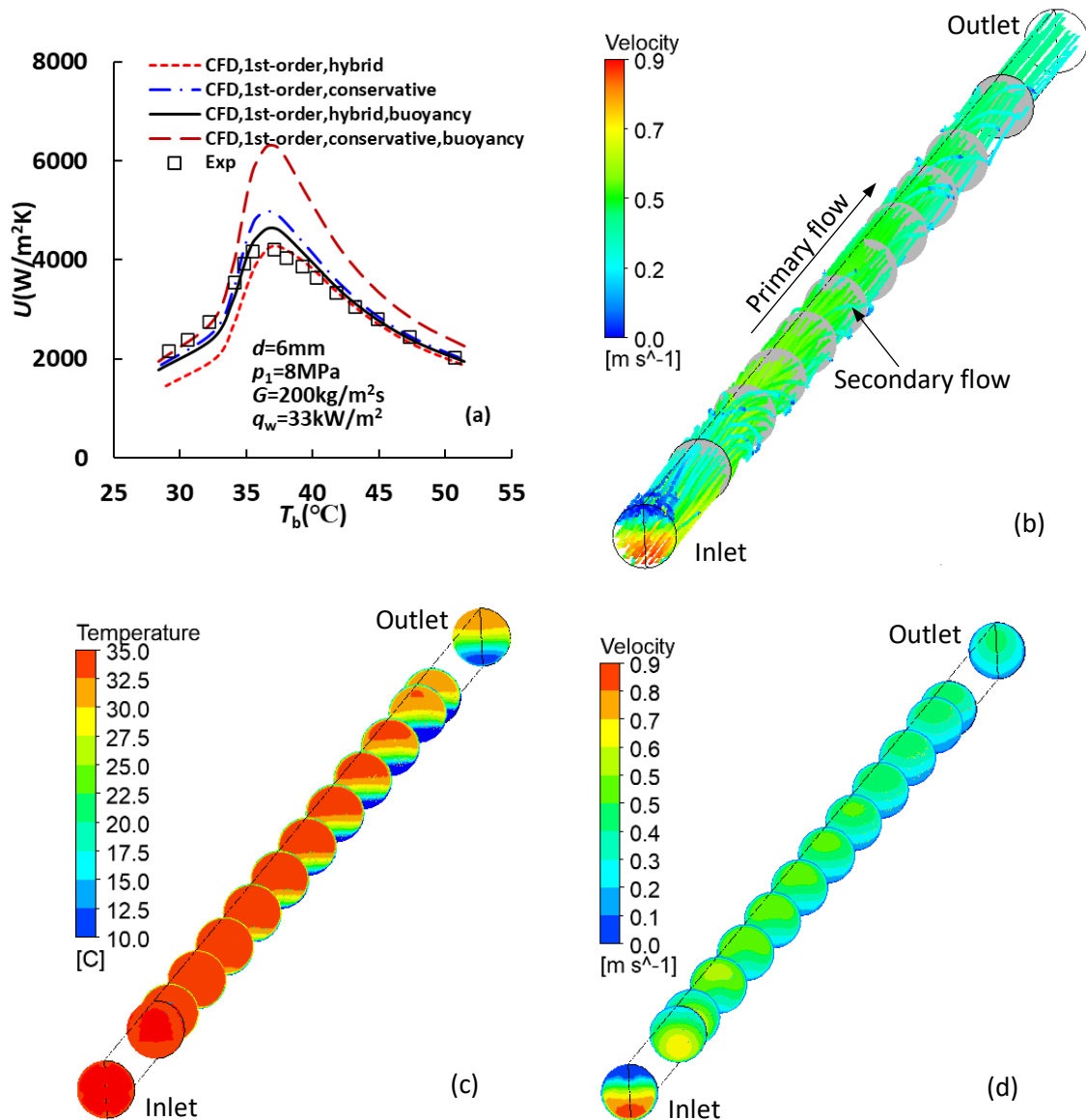


Figure 13 The MHTC curves (a), the secondary flow near the tube wall (b), temperature contour (c) and velocity contour (d) predicted when the buoyancy effect is considered in the case: $d=6mm$, $p_1=8MP$, $G=200kg/m^2s$ and $q_w=33kW/m^2$, the experimental data after [15], in(b), $T_1=35^{\circ}C$

4.6 Limitations

In the CFD simulations, a single-phase flow model is adopted. In this circumstance, the SCO_2 is still treated as a gas in ANSYS CFX even though a few input conditions in the CFD simulations enters into the liquid state, shown in Figure 14. This fact may affect the accuracy of MHTC prediction, but it needs further confirmation with other flow models. Ideally, two-phase flow models, which include a mixture of liquid CO_2 and vapour CO_2 as well as a thermodynamic phase-change model, should be employed at least on the left-hand side of the Λ -shaped MHTC curve. The state of CO_2 is determined by the phase-change model based on

known CO₂ pressure and temperature and bubble nucleation as well as the other thermophysical and transport property constants.

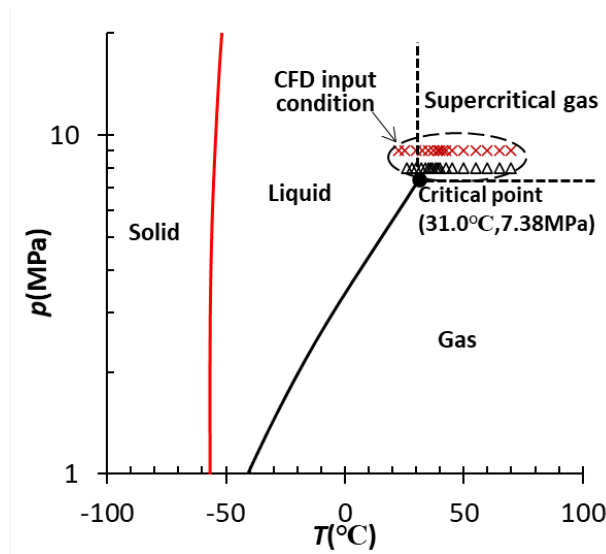


Figure 14 The SCO₂ pressure-temperature chart and SCO₂ input conditions in the CFD simulations

In the CFD simulations, a constant wall heat flux was applied to the tube wall. This wall heat flux is not the true heat flux across the tube wall but an equivalent one to the uneven wall heat flux calculated by using 1D conductive heat transfer formulas. Accordingly, the SCO₂ bulk temperature and tube wall temperature predicted by CFD simulations were averaged to obtain an MHTC. The agreement between the predicted and the measured MHTCs makes sense in 1D conductive heat transfer only. A comparison of variable heat transfer coefficients in a tube-in-tube HX requires further experimental data associated with wall temperature longitudinal profile, cooling water flow rate, inlet and outlet temperatures. A very recent experimental work provides quite useful information about cooling water inlet and outlet temperatures to validate forced convective heat transfer simulations in a tube-in-tube heat exchanger by employing complete geometrical models [31].

In Eq. (12), the turbulent Prandtl number Pr_t is selected to be 0.9 as usual based on the Reynolds analogy where the similarity between turbulent transport of momentum and that of heat is postulated. This hypothesis leads to the Reynolds-averaged fluctuating terms $\overline{u_i' T'}$ in the energy equation is proportional to the time-averaged temperature gradients $\partial T / \partial x_i$ with a constant:

$$\overline{u_i' T'} = -\zeta_t \frac{\partial T}{\partial x_i}, \quad \zeta_t = \frac{\mu_t}{\rho Pr_t} \quad (9)$$

where u_i' are the fluctuation of fluid velocity components u_i , T' is fluctuation of fluid temperature, ζ_t is turbulent thermal diffusivity. Pr_t profile in the region of $y^+ < 6$ can influence heat transfer coefficient and wall temperature. To achieve better agreement with

experimental data a number of empirical correlations of Pr_t have been proposed for fully developed turbulent of water or air in a pipe [32] [33] [34] [35] [36] [37] [38]. For forced convective heat transfer associated with SCO₂, it is possible that the overproduction in heat transfer coefficient near the pseudocritical point is due to the Pr_t profile across a boundary layer [39]. In this context, a few empirical Pr_t profiles have been developed in the literature [39] [40] [41] [42]. In the present paper, $Pr_t = 0.9$ was used in all CFD simulations. Nevertheless, other variable Pr_t profiles are worth being attempted in SCO₂ heat transfer in tube-in-tube HXs in the future.

5 Conclusion

Two geometrical models of an experimental counter-flow tube-in-tube heat exchanger, i.e., complete model and sole tube model, were generated, Then the forced convective heat transfer of SCO₂ flowing the heat exchanger was simulated by using the 3D RANS method with SST turbulence model in ANSYS CFX. It was shown that the sole tube geometrical model is viable for CFD heat transfer simulations when the known wall heat transfer flux across the wall between SCO₂ and cooling water is given. Except near the pseudocritical point, the mean heat transfer coefficient of SCO₂ flows based on the SST model demonstrates better agreement with the experimental data than the other turbulence models. Also, the effects of inlet pressure, mass flux, tube diameter and wall heat flux on the SCO₂ mean heat transfer coefficient predicted with the adopted flow models and numerical methods are found similar to those obtained in experiments.

Furthermore, the numerical discretisation scheme of the advection terms in the SST model and conservative and hybrid values in CFX-Post for the wall temperature have a strong influence on the mean heat transfer coefficient. The 1st-order scheme and the wall temperature of conservative values can lead to a better prediction in the mean heat transfer coefficient. The mean heat transfer coefficient predicted with the 2nd-order (high resolution) scheme and the wall temperature of hybrid values in CFX-Post is similar to that obtained with the 1st-order scheme and the wall temperature of conservative values. In addition, the Richardson number for assessing the buoyancy effect in forced convective heat transfer in a horizontal tube is in a range of 0.0014-0.23 among the cases studied. In the case with the largest Richardson number, the buoyancy effect makes a dominant contribution to the mean heat transfer coefficient. In this context, the 1st-order scheme and the wall temperature in terms of hybrid values can improve the accuracy of prediction in mean heat transfer coefficient because of the spiral secondary flows induced by the variable density of SCO₂ across the tube cross-section under the action of acceleration of gravity.

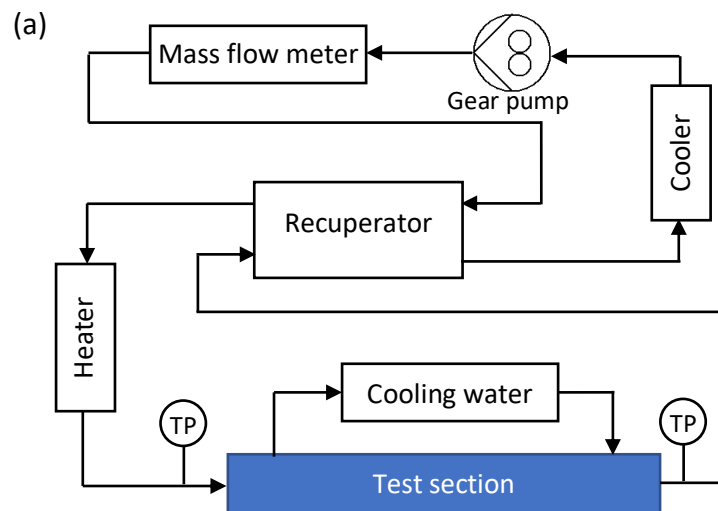
Acknowledgment

The authors would like to acknowledge the financial support provided by the Engineering and Physical Sciences Research Council (EPSRC) in the UK [grant numbers EP/T022701/1, EP/P028829/1, EP/V042033/1], and the European Commission [grant number 01007976]. Prof Zhibin Yu and Dr Yi Wang provided language editing and proof reading.

Appendix A The Selected Existing Experiment

The schematic of the experimental set-up and the axial-cross-sectional view of the SCO₂ counter-flow tube-in-tube HX in [15] are illustrated in Fig. A.1a. The gear pump delivers liquid CO₂ to the heater where the CO₂ is heated and turns into SCO₂. It then enters the test section, and the tube-in-tube HX, and is cooled by water flowing outside the wall of the inner (hot) tube. The cooled SCO₂ is discharged from the exchanger and returns to the pump through a cooler. The cooled SCO₂ is discharged from the exchanger and returns to the pump through a cooler.

The test section is a 500mm long horizontal counter-flow tube-in-tube HX. The hot SCO₂ flows in the inner tube with 1mm thickness and 6mm inner diameter from the left to the right. A stream of water runs in the annulus between the outer tube (12mm inner diameter) and the inner tube from the right to the left. The flowing water takes heat away from the hot SCO₂, and outward heat flux is generated across the wall of the inner tube during this process.



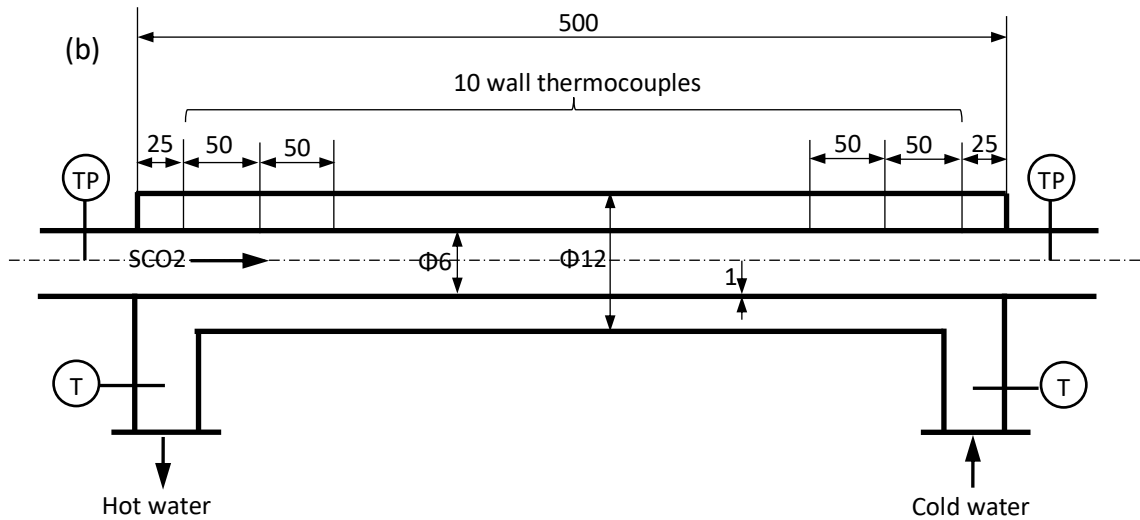


Figure A.1 The schematic of test-loop (a) and axial-cross-sectional view of the tested SCO₂ counter-flow tube-in-tube HX (b) in [15], T-thermocouple, TP-thermal and pressure sensors, the pictures are adapted from [15]

The SCO₂ pressure and temperature were measured at both the inlet and outlet of the inner tube; likewise, the water temperature was measured at both the inlet and outlet of the annulus. The SCO₂ mass flow rate was measured but the cooling water flow rate was overlooked. The temperature at the outside wall of the inner tube was measured at ten points evenly distributed as shown Fig. A.1b. The inside wall temperature of the inner tube at the 10 locations were calculated from the corresponding outside wall temperature by using 1D conductive heat transfer equations. The mean wall temperature was the arithmetic mean of the ten estimated inside wall temperatures. The SCO₂ mean bulk temperature in the inner tube was the arithmetic mean of the measured SCO₂ temperatures at the inlet and outlet of the inner tube. The respective experimental conditions in [15] are listed in Table A.1, and will be used in the CFD simulations in the paper.

Table A.1 The cases studied in the SCO₂ flow and heat transfer simulations

Inner diameter, d (mm)	Mass flux, G (kg/m ² s)	Wall heat flux, q_w (kW/m ²)	Inlet pressure, p_1 (MPa)	Inlet temperature, T_1 (°C)
4	800	12	9	23.5-65
6	200	6	8	26-65
		12		
		24		
		33		
	400	12		

Appendix B The Flow and Heat Transfer Models

For subsonic, compressible SCO₂, the 3D RANS equations and energy equation with eddy viscosity of turbulence models are written as [16]

$$\frac{\partial \rho}{\partial t} + \frac{\partial}{\partial x_j} (\rho u_j) = 0 \quad (\text{B.1})$$

$$\frac{\partial}{\partial t} (\rho u_i) + \frac{\partial}{\partial x_j} (\rho u_i u_j) = -\frac{\partial}{\partial x_i} \left(p + \frac{2}{3} \rho k \right) + \frac{\partial}{\partial x_j} \left[(\mu + \mu_t) \left(\frac{\partial u_i}{\partial x_j} + \frac{\partial u_j}{\partial x_i} \right) \right] + \rho S_i \quad (\text{B.2})$$

$$\frac{\partial}{\partial t} \left[\rho \left(h + \frac{1}{2} u_i u_i + k \right) \right] - \frac{\partial p}{\partial t} + \frac{\partial}{\partial x_j} \left[\rho u_j \left(h + \frac{1}{2} u_i u_i + k \right) \right] = \frac{\partial}{\partial x_j} \left(\lambda \frac{\partial T}{\partial x_j} + \frac{\mu_t}{Pr_t} \frac{\partial h}{\partial x_j} \right) + S_E \quad (\text{B.3})$$

where ρ is the density of SCO₂, t is time, u_i and u_j are the Reynolds time-averaged velocity of SCO₂ in the coordinate x_i and x_j directions, respectively; i and j are the coordinate index, $i, j=1,2,3$; p is the pressure of SCO₂, k is the turbulence kinetic energy, $k = \frac{1}{2} \overline{u_i'^2}$, u_i' is turbulent fluctuation velocity of SCO₂, μ is laminar dynamic viscosity of SCO₂, μ_t is turbulent eddy viscosity, S_i is the specific body force, $S_i=0$ is held here, h is the enthalpy of SCO₂, λ is the thermal conductivity of SCO₂, T is the temperature of SCO₂, Pr_t is the turbulent Prandtl number, $Pr_t=0.9$, S_E is the source term of energy, $S_E=0$ here; ρ , μ and λ are given by the RGP table.

CFD heat transfer simulations of SCO₂ require to resolve the viscous sublayer in a boundary layer to achieve correct heat transfer coefficient and wall temperature. Initially, additional low-Reynolds number models for the viscous sublayer were used based on the standard $k - \varepsilon$ model [43] [44] [45] [3] [4] with very fine mesh near the wall, i.e. $y^+ (= \sqrt{\tau_w / \rho} y_n / \nu \leq 2)$, τ_w is the shear stress at the wall, y_n is the distance to the nearest wall from the first mesh layer, ν is the kinematic viscosity of SCO₂, $\nu = \mu / \rho$.

Further, the Wilcox $k - \omega$ turbulence model was applied to SCO₂ heat transfer simulations [13]. The Wilcox $k - \omega$ model employs a wall function in which the friction velocities and ω values for the sublayer and the turbulence dominated log-law layer are analytically blended [46]. As a result, a low-Reynolds number model is not needed, and the simulated results are less dependent on y^+ values. The turbulent eddy viscosity, however, is overpredicted because the transport of the turbulent shear stress is not considered, and the predicted heat transfer coefficients do not agree with the observations well [13].

Recently, the SST turbulence model has played an increasingly important role in SCO₂ heat transfer simulations [6] [7] [8] [9] [10]. The SST model is a blended version of the Wilcox $k - \omega$ model and the standard $k - \varepsilon$ model. In the SST model, the flow near the wall is handled by the Wilcox $k - \omega$ model, but the core flow is simulated by the standard $k - \varepsilon$ model. Taking into account the transport of the shear stress, the overprediction of turbulent eddy viscosity is suppressed in the Wilcox $k - \omega$ model [46]. The Wilcox $k - \omega$ model is expressed as [16]

$$\frac{\partial}{\partial t}(\rho k) + \frac{\partial}{\partial x_j}(\rho u_j k) = \frac{\partial}{\partial x_j} \left[\left(\mu + \frac{\mu_t}{\sigma_{k1}} \right) \frac{\partial k}{\partial x_j} \right] + P_k - \beta_k \rho k \omega + P_{kb} \quad (\text{B.4})$$

$$\frac{\partial}{\partial t}(\rho \omega) + \frac{\partial}{\partial x_j}(\rho u_j \omega) = \frac{\partial}{\partial x_j} \left[\left(\mu + \frac{\mu_t}{\sigma_{\omega 1}} \right) \frac{\partial \omega}{\partial x_j} \right] + \frac{\alpha_1}{\nu_t} P_k - \beta_1 \rho k \omega^2 + P_{\omega b} \quad (\text{B.5})$$

where σ_{k1} , β_k , $\sigma_{\omega 1}$, α_1 and β_1 are the model constants, $\sigma_{k1} = \sigma_{\omega 1} = 2$, $\alpha_1 = 5/9$, $\beta_k = 0.09$, $\beta_1 = 0.075$; P_{kb} and $P_{\omega b}$ are the buoyancy production term in the k -equation and ω -equation, respectively; since the SCO2 inlet temperature is low, the two production terms are ignored. The ω -transformed standard k - ε model is written as:

$$\frac{\partial}{\partial t}(\rho k) + \frac{\partial}{\partial x_j}(\rho u_j k) = \frac{\partial}{\partial x_j} \left[\left(\mu + \frac{\mu_t}{\sigma_{k2}} \right) \frac{\partial k}{\partial x_j} \right] + P_k - \beta_k \rho k \omega + P_{kb} \quad (\text{B.6})$$

$$\frac{\partial}{\partial t}(\rho \omega) + \frac{\partial}{\partial x_j}(\rho u_j \omega) = \frac{\partial}{\partial x_j} \left[\left(\mu + \frac{\mu_t}{\sigma_{\omega 2}} \right) \frac{\partial \omega}{\partial x_j} \right] + \frac{\alpha_2}{\nu_t} P_k - \beta_2 \rho k \omega^2 + \frac{2\rho}{\sigma_{\omega 2} \omega} \frac{\partial k}{\partial x_j} \frac{\partial \omega}{\partial x_j} + P_{\omega b} \quad (\text{B.7})$$

where σ_{k2} , $\sigma_{\omega 2}$, α_2 and β_2 are the model constants, $\sigma_{k2} = 1$, $\sigma_{\omega 2} = 1/0.856$, $\alpha_2 = 0.44$, $\beta_2 = 0.0828$.

Introducing a blending function F_1 and combining Eq.(B.4) and (B.6), Eq.(B.5) and (B.7) in the manner such as $F_1 \times \text{Eq.}(B.4) + (1-F_1) \times \text{Eq.}(B.6)$ and $F_1 \times \text{Eq.}(B.5) + (1-F_1) \times \text{Eq.}(B.7)$, respectively, then a blended k - ω model is achieved as:

$$\frac{\partial}{\partial t}(\rho k) + \frac{\partial}{\partial x_j}(\rho u_j k) = \frac{\partial}{\partial x_j} \left[\left(\mu + \frac{\mu_t}{\sigma_{k3}} \right) \frac{\partial k}{\partial x_j} \right] + P_k - \beta_k \rho k \omega + P_{kb} \quad (\text{B.8})$$

$$\frac{\partial}{\partial t}(\rho \omega) + \frac{\partial}{\partial x_j}(\rho u_j \omega) = \frac{\partial}{\partial x_j} \left[\left(\mu + \frac{\mu_t}{\sigma_{\omega 3}} \right) \frac{\partial \omega}{\partial x_j} \right] + \frac{\alpha_3}{\nu_t} P_k - \beta_3 \rho k \omega^2 + (1 - F_1) \frac{2\rho}{\sigma_{\omega 2} \omega} \frac{\partial k}{\partial x_j} \frac{\partial \omega}{\partial x_j} + P_{\omega b} \quad (\text{B.9})$$

where σ_{k3} , $\sigma_{\omega 3}$, α_3 and β_3 are the blended model constants, expressed as $\sigma_{k3} = F_1 \sigma_{k1} + \beta_1 (1 - F_1) \sigma_{k2}$, $\sigma_{\omega 3} = F_1 \sigma_{\omega 1} + (1 - F_1) \sigma_{\omega 2}$, $\alpha_3 = F_1 \alpha_1 + (1 - F_1) \alpha_2$, and $\beta_3 = F_1 \beta_1 + (1 - F_1) \beta_2$; F_1 is a blending function between the Wilcox k - ω model and the standard k - ε model, especially, $F_1 = 1$ at the wall, $F_1 = 0$ in the core flow, and $0 < F_1 < 1$ between the wall and the core flow. A specific expression for F_1 is written as [16] [46]:

$$F_1 = \tanh(\xi_1^4), \xi_1 = \min \left(\max \left(\frac{\sqrt{k}}{\beta_k \omega y_n}, \frac{500\nu}{y_n^2 \omega} \right), \frac{4\rho k}{\xi_2 \sigma_{\omega 2} y^2} \right), \xi_2 = \max \left(\frac{2\rho}{\sigma_{\omega 2} \omega} \frac{\partial k}{\partial x_j} \frac{\partial \omega}{\partial x_j}, 1.0 \times 10^{-10} \right) \quad (\text{B.10})$$

where y_n is the distance to the nearest wall.

In ANSYS CFX, the model expressed by Eqs. (B.8)-(B.10) is called the baseline (BLS) k - ω model [16]. This model usually overpredicts the turbulent eddy-viscosity. To take the SST into account, the eddy-viscosity should be limited in some way. In [46], a mathematical expression was proposed to help address the overprediction of the eddy-viscosity, which reads as:

$$\mu_t = \min \left(\frac{\rho k}{\omega}, \frac{a\rho k}{S F_2} \right), \gamma = \sqrt{2\gamma_{ij}\gamma_{ij}}, \gamma_{ij} = \frac{1}{2} \left(\frac{\partial u_i}{\partial x_j} + \frac{\partial u_j}{\partial x_i} \right), F_2 = \tanh(\xi_2^2), \xi_3 = \max \left(\frac{2\sqrt{k}}{\beta_k \omega y_n}, \frac{500\nu}{y_n^2 \omega} \right) \quad (\text{B.11})$$

where a is model constant, $a = 0.31$, γ is the magnitude of the strain rate and γ_{ij} represents the strain rate tensor; F_2 and ξ_3 are auxiliary variables. In ANSYS CFX, the model composed by

Eqs. (B.7)-(B.10) is the SST model. Note that the SST is not considered explicitly but implicitly by limiting the eddy-viscosity in the model.

In the SST model, the low-Reynolds number model for the viscous sublayer is replaced with a blended wall function, which is called as the Automatic Near-Wall Treatment in ANSYS CFX. It is a function of $y^+ (=u_\tau y_n/\mu)$, where u_τ denotes the friction velocity of SCO2 at the wall. Based on the solutions in the linear and the logarithmic near-wall regions, the blended wall function is focused on both ω and u_τ , and written as [46]:

$$\begin{cases} \omega_1 = \sqrt{\omega_{vis}^2 + \omega_{log}^2}, \omega_{vis} = \frac{6\nu}{\beta_1 y^2}, \omega_{log} = \frac{u_\tau}{a_1 \kappa y} \\ u_\tau = \sqrt[4]{(u_\tau^{vis})^4 + (u_\tau^{log})^4}, u_\tau^{vis} = \frac{u_1}{y^+}, u_\tau^{log} = \frac{u_n}{\frac{1}{\kappa} \ln(y^+) + B} \end{cases} \quad (\text{B.12})$$

where ω_{vis} and ω_{log} are the ω values calculated by the solutions in the linear and the logarithmic near-wall regions, ω_1 is the total ω near wall, u_τ^{vis} and u_τ^{log} are the friction velocities at a wall by using the solutions in the sublayer and log-law layers, u_n is the fluid velocity near the wall, B is a constant, $B=5.2$ for hydraulically smooth walls, u_τ is the resultant friction velocity at the wall, and related to the wall shear stress with $\tau_w = \rho u_\tau^2$; κ is the von Kármán constant, $\kappa=0.41$. The fluxes in the momentum equation and the k -equation at wall are detailed in [16].

In the sublayer and log-law regions, the following empirical expression in [47] is employed in CFX to determine the dimensionless temperature in convective heat transfer presented in [46]:

$$\begin{cases} T^+ = Pr y^+ e^{-\Gamma} + [0.1 \ln(y^+) + \beta] e^{-1/\Gamma}, \Gamma = \frac{0.01(Pr y^+)^4}{1+5Pr^3 y^+} \\ q_w = \frac{\rho C_p u_\tau}{T^+} (T_w - T_n), Pr = \frac{\mu C_p}{\lambda}, \beta = (3.85 Pr^{1/3} - 1.3) + 0.1 \ln(Pr) \end{cases} \quad (\text{B.13})$$

where Γ is the auxiliary variable of Pr and y^+ , q_w is the wall heat flux, C_p is the specific heat capacity of SCO2, T^+ is the dimensionless temperature in the boundary layer, T_w is the wall temperature, T_n is the SCO2 temperature in the first mesh layer, β is an auxiliary variable of the model, Pr is the SCO2 Prandtl number; the SCO2 property constants, ρ , μ , C_p and λ should be the local values in the first mesh layer. Based on Eqs. (B.12) and (B.13), the flow and heat transfer variables at the wall such as shear stress, wall temperature or heat flux can be calculated.

References

- [1] Anonymous, "The emerging cold economy," *The Carbon Trust*, pp. 1-18, 2015.

- [2] W. Li and Z. Yu, "Heat exchangers for cooling supercritical carbon dioxide and heat transfer enhancement: A review and assessment," *Energy Reports*, vol. 7, pp. 4085-4105, 2021.
- [3] Z. Du, W. Lin and A. Gu, "Numerical investigation of cooling heat transfer to supercritical CO₂ in a horizontal circular tube," *Journal of Supercritical Fluids*, vol. 55, pp. 116-121, 2010.
- [4] J. Wang, Z. Guan, H. Gurgenci and et al, "Computational investigations of heat transfer to supercritical CO₂ in a large horizontal tube," *Energy Conversion and Management*, vol. 157, pp. 536-548, 2018.
- [5] J. Wang, Z. Guan, H. Gurgenci and et al, "Numerical study on cooling heat transfer of turbulent supercritical CO₂ in large horizontal tubes," *International Journal of Heat and Mass Transfer*, vol. 126, pp. 1002-1019, 2018.
- [6] Z. Li, A. Kruizenga, M. Anderson and et al, "Development of a new forced convection heat transfer correlation for CO₂ in both heating and cooling modes at supercritical pressures," *International Journal of Thermal Sciences*, vol. 50, pp. 2430-2442, 2011.
- [7] M. Xiang, J. Guo, X. Huai and et al, "Thermal analysis of supercritical pressure CO₂ in horizontal tubes under cooling condition," *Journal of Supercritical Fluids*, vol. 130, pp. 389-398, 2017.
- [8] Z. Yang, W. Chen and M. K. Chyu, "Numerical study on the heat transfer enhancement of supercritical CO₂ in vertical ribbed tubes," *Applied Thermal Engineering*, vol. 145, pp. 705-715, 2018.
- [9] S. Zhang, X. Xu, C. Liu and et al, "The buoyancy force and flow acceleration effects of supercritical CO₂ on the turbulent heat transfer characteristics in heated vertical helically coiled tube," *International Journal of Heat and Mass Transfer*, vol. 125, pp. 274-289, 2018.
- [10] Y. Tu and Y. Zeng, "Flow and heat transfer characteristics study of supercritical CO₂ in horizontal semicircular channel for cooling process," *Case Studies in Thermal Engineering*, vol. 21, p. 100691, 2020.
- [11] P. Forooghi and K. Hooman, "Numerical study of turbulent convection in inclined pipes with significant buoyancy influence," *International Journal of Heat and Mass Transfer*, vol. 61, pp. 310-322, 2013.
- [12] S. H. Han, Y. D. Choi, J. K. Shin and et al, "Turbulent heat transfer of supercritical carbon dioxide in square cross-sectional duct flow," *Journal of Mechanical Science and Technology*, vol. 22, pp. 2563-2577, 2008.
- [13] M. Yang, "Numerical study on the heat transfer of carbon dioxide in horizontal straight tubes under supercritical pressure," *PLoS ONE*, vol. 11, no. 7, pp. 1-24, 2016.
- [14] P. Asinari, "Numerical prediction of turbulent convective heat transfer in mini/micro channels for carbon dioxide at supercritical pressure," *International Journal of Heat and Mass Transfer*, vol. 48, pp. 3864-3879, 2005.
- [15] C. Dang and E. Hihara, "In-tube cooling heat transfer of supercritical carbon dioxide: Part 1. Experimental measurement," *International Journal of Refrigeration*, vol. 27, pp. 736-747, 2004.

- [16] ANSYS, ANSYS CFX-Solver Theory Guide, Canonsburg: ANSYS, Inc. , 2011.
- [17] ANSYS, ANSYS CFX-Solver Modeling Guide, Canonsburg: ANSYS, Inc., 2011.
- [18] T. Ma, W. X. Chu, X. Y. Xu and e. al, "An experimental study on heat transfer between supercritical carbon dioxide and water near the pseudo-critical temperature in a double pipe heat exchanger," *International Journal of Heat and Mass Transfer*, vol. 93, pp. 379-387, 2016.
- [19] S. M. Liao and T. S. Zhao, "An experimental investigation of convection heat transfer to supercritical carbon dioxide in miniature tubes," *International Journal of Heat and Mass Transfer*, vol. 45, pp. 5025-5034, 2002.
- [20] G. Liu, Y. Huang, J. Wang and et al, "Effect of buoyancy and flow acceleration on heat transfer of supercritical CO₂ in natural circulation loop," *International Journal of Heat and Mass Transfer*, vol. 91, pp. 640-646, 2015.
- [21] S. Liu, Y. Huang, G. Liu and et al, "Improvement of buoyancy and acceleration parameters for forced and mixed convective heat transfer to supercritical fluids flowing in vertical tubes," *International Journal of Heat and Mass Transfer*, vol. 106, pp. 1144-1156, 2017.
- [22] R. N. Xu, F. Luo and P. X. Jiang, "Buoyancy effects on turbulent heat transfer of supercritical CO₂ in a vertical mini-tube based on continuous wall temperature measurements," *International Journal of Heat and Mass Transfer*, vol. 110, pp. 576-586, 2017.
- [23] C. Yang, J. Xu, X. Wang and et al, "Mixed convective flow and heat transfer of supercritical CO₂ in circular tubes at various inclination angles," *International Journal of Heat and Mass Transfer*, vol. 64, pp. 212-223, 2013.
- [24] X. Chu and E. Laurien, "Flow stratification of supercritical CO₂ in a heated horizontal pipe," *Journal of Supercritical Fluids*, vol. 116, pp. 172-189, 2016.
- [25] D. E. Kim and M. H. Kim, "Two layer heat transfer model for supercritical fluid flow in a vertical tube," *Journal of Supercritical Fluids*, vol. 58, pp. 15-25, 2011.
- [26] J. D. Jackson, "Fluid flow and convective heat transfer to fluids at supercritical pressure," *Nuclear Engineering and Design*, vol. 264, pp. 24-40, 2013.
- [27] N. Kline, F. Feuerstein and S. Tavoularis, "Onset of heat transfer deterioration in vertical pipe flows of CO₂ at supercritical pressures," *International Journal of Heat and Mass Transfer*, vol. 118, pp. 1056-1068, 2018.
- [28] P. X. Jiang, Z. C. Wang and R. N. Xu, "A modified buoyancy effect correction method on turbulent convection heat transfer of supercritical pressure fluid based on RANS model," *International Journal of Heat and Mass Transfer*, vol. 127, pp. 257-267, 2018.
- [29] Z. Yang, X. Cheng, X. Zheng and et al, "Numerical investigation on heat transfer of the supercritical fluid upward in vertical tube with constant wall temperature," *International Journal of Heat and Mass Transfer*, vol. 128, pp. 875-884, 2019.

- [30] J. D. Jackson, M. A. Cotton and B. P. Axcell, "Studies of mixed convection in vertical tubes," *International Journal of Heat and Fluid Flow*, vol. 10, no. 1, pp. 2-15, 1989.
- [31] A. Wahl, R. Mertz, E. Laurien and et al, "Heat transfer correlation for sCO₂ cooling in a 2 mm tube," *Journal of Supercritical Fluids*, vol. 173, p. 105221, 2021.
- [32] T. Y. Na and I. S. Habib, "Heat transfer in turbulent pipe flow based on a new mixing length model," *Applied Scientific Research*, vol. 28, pp. 302-314, 1973.
- [33] R. A. Antonia and J. Kim, "Turbulent Prandtl number in the near-wall region of a turbulent channel flow," *International Journal of Heat Mass Transfer*, vol. 34, no. 7, pp. 1905-1908, 1991.
- [34] K. Rup and P. Wais, "An application of the k- ϵ model with variable Prandtl number to heat transfer computations in air flows," *Heat and Mass Transfer*, vol. 34, pp. 503-508, 1999.
- [35] K. Rup and M. Soczowka, "An improved low Reynolds number k- ϵ for heat transfer calculations," *Forschung im Ingenieurwesen*, vol. 65, pp. 225-235, 2000.
- [36] V. A. Kurganov and I. V. Maslakova, "A modified model for the calculation of fully developed heat transfer and drag in tubes under conditions of turbulent flow of gases with varying physical properties," *High Temperature*, vol. 41, no. 6, pp. 790-800, 2003.
- [37] C. L. Liu, H. R. Zhu and J. T. Bai, "New development of the turbulent Prandtl number models for the computation of film cooling effectiveness," *International Journal of Heat and Mass Transfer*, vol. 54, pp. 874-886, 2011.
- [38] A. Shams and A. De Santis, "Towards the accurate prediction of the turbulent flow and heat transfer in low-Prandtl fluids," *International Journal of Heat and Mass Transfer*, vol. 130, pp. 290-303, 2019.
- [39] Y. Y. Bae, "A new formulation of variable turbulent Prandtl number for heat transfer to supercritical fluids," *International Journal of Heat and Mass Transfer*, vol. 92, pp. 792-806, 2016.
- [40] M. Mohseni and M. Bazargan, "A new correlation for the turbulent Prandtl number in upward rounded tubes in supercritical fluid flows," *ASME Journal of Heat Transfer*, vol. 138, p. 081701, 2016.
- [41] G. Tang, H. Shi, Y. Wu and et al, "A variable turbulent Prandtl number model for simulating supercritical pressure CO₂ heat transfer," *International Journal of Heat and Mass Transfer*, vol. 102, pp. 1082-1092, 2016.
- [42] R. Tian, X. Dai, D. Wang and e. al, "Study of variable turbulent Prandtl number model for heat transfer to supercritical fluids in vertical tubes," *Journal of Thermal Science*, vol. 27, no. 3, pp. 213-222, 2018.
- [43] C. Dang and E. Hihara, "In-tube cooling heat transfer of supercritical carbon dioxide: Part 2. Comparison of numerical calculation with different turbulence models," *International Journal of Refrigeration*, vol. 27, pp. 748-760, 2004.

- [44] S. He, W. S. Kim, P. X. Jiang and et al, "Simulation of mixed convection heat transfer to carbon dioxide at supercritical pressure," *Proc. Instn Mech. Engrs, Part C: Journal of Mechaniccal Engineering Science*, vol. 218, no. 11, pp. 1281-1296, 2004.
- [45] W. S. Kim, J. D. Jackson, S. He and et al, "Performance of a variety of low Reynolds number turbulence models applied to mixed convection heat transfer to air flowing upwards in a vertical tube," *Proc. Instn Mech. Engrs, Part C: Journal of Mechaniccal Engineering Science*, vol. 218, no. 11, pp. 1361-1372, 2004.
- [46] F. Menter, J. C. Ferreira, T. Esch and et al, "The SST turbulence model with improved wall treatment for heat transfer predictions in gas turbines," in *Proceedings of the International Gas Turbine Congress*, Tokyo, 2003.
- [47] B. A. Kader, "Temperature and concentration profiles in fully turbulent boundary layers," *International Journal of Heat and Mass Transfer*, vol. 24, no. 9, pp. 1541-1544, 1981.